Article

Cell Systems

Deciphering the signaling network of breast cancer improves drug sensitivity prediction

Graphical abstract

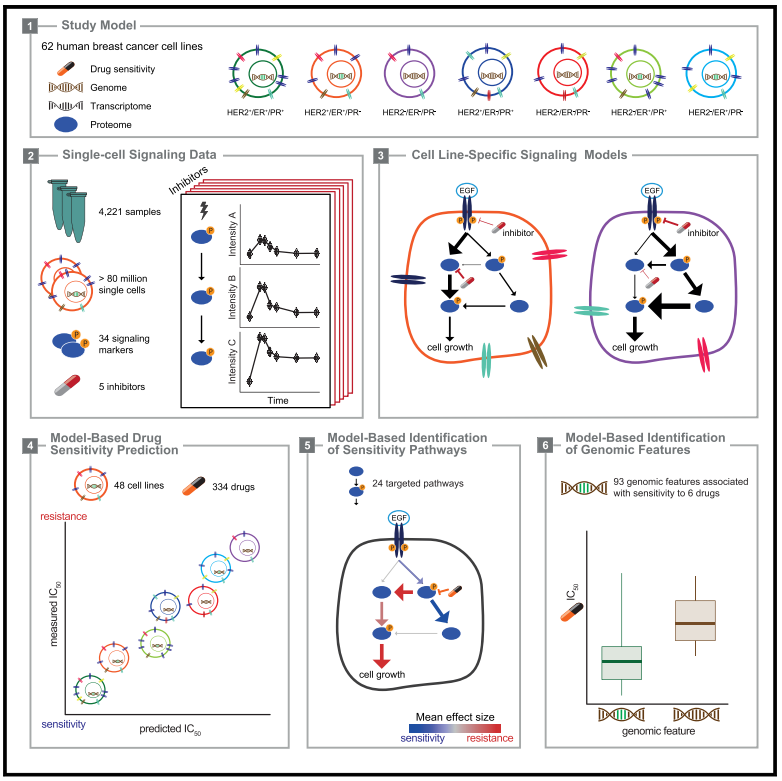

Highlights

- Mass cytometry-based single-cell signaling dataset on 62 breast cancer cell lines
- Single-cell signaling features and mechanistic models predicted drug sensitivity
- Signaling models probed drug resistance and sensitivity mechanisms
- Drug sensitivity-predictive genomic features identified via signaling phenotypes

Authors

Marco Tognetti, Attila Gabor, Mi Yang, ..., Paola Picotti, Julio Saez-Rodriguez, Bernd Bodenmiller

Correspondence

bernd.bodenmiller@uzh.ch

In brief

Signaling models based on multiplex single-cell mass cytometry improve predictions of drug sensitivity in breast cancer cell lines and probe mechanisms of drug sensitivity and resistance.

Tognetti et al., 2021, Cell Systems *12*, 401–418
May 19, 2021
https://doi.org/10.1016/j.cels.2021.04.002

CellPress

Cell Systems

CellPress
OPEN ACCESS

Article

Deciphering the signaling network of breast cancer improves drug sensitivity prediction

Marco Tognetti,[1,2,3,4] Attila Gabor,[5,6] Mi Yang,[6,7] Valentina Cappelletti,[3] Jonas Windhager,[1,2,8] Oscar M. Rueda,[9] Konstantina Charmpi,[10] Elham Esmaeilishirazifard,[9,11] Alejandra Bruna,[9] Natalie de Souza,[1,3] Carlos Caldas,[9,12] Andreas Beyer,[10,13,14] Paola Picotti,[3] Julio Saez-Rodriguez,[5,6] and Bernd Bodenmiller[1,2,15,*]

[1]Department of Quantitative Biomedicine, University of Zürich, 8057 Zurich, Switzerland
[2]Institute of Molecular Life Sciences, University of Zürich, 8057 Zurich, Switzerland
[3]Institute of Molecular Systems Biology, ETH Zürich, 8093 Zurich, Switzerland
[4]Molecular Life Science PhD Program, Life Science Zürich Graduate School, ETH Zürich and University of Zürich, 8057 Zurich, Switzerland
[5]Institute for Computational Biomedicine, Faculty of Medicine, Heidelberg University, 69117 Heidelberg, Germany
[6]Joint Research Centre for Computational Biomedicine (JRC-COMBINE), Faculty of Medicine, RWTH Aachen University, 52074 Aachen, Germany
[7]Faculty of Biosciences, Heidelberg University, 69117 Heidelberg, Germany
[8]Systems Biology PhD Program, Life Science Zürich Graduate School, ETH Zürich and University of Zürich, 8093 Zürich, Switzerland
[9]Department of Oncology and Cancer Research UK Cambridge Institute, Li Ka Shing Centre, University of Cambridge, Cambridge CB2 0RE, UK
[10]Cologne Excellence Cluster Cellular Stress Response in Aging-Associated Diseases (CECAD), Medical Faculty and Faculty of Mathematics and Natural Sciences, University of Cologne, 50923 Cologne, Germany
[11]Bioscience, R&D Oncology, Astra Zeneca, Cancer Research UK Cambridge Institute, Cambridge CB2 0RE, UK
[12]Cambridge Breast Unit, NIHR Cambridge Biomedical Research Centre and Cambridge Experimental Cancer Medicine Centre at Cambridge University Hospitals NHS Foundation Trust, Cambridge CB2 0QQ, UK
[13]Center for Molecular Medicine (CMMC), University of Cologne, 50923 Cologne, Germany
[14]Institute for Genetics, Faculty of Mathematics and Natural Sciences, University of Cologne, 50923 Cologne, Germany
[15]Lead contact
*Correspondence: bernd.bodenmiller@uzh.ch
https://doi.org/10.1016/j.cels.2021.04.002

SUMMARY

One goal of precision medicine is to tailor effective treatments to patients' specific molecular markers of disease. Here, we used mass cytometry to characterize the single-cell signaling landscapes of 62 breast cancer cell lines and five lines from healthy tissue. We quantified 34 markers in each cell line upon stimulation by the growth factor EGF in the presence or absence of five kinase inhibitors. These data—on more than 80 million single cells from 4,000 conditions—were used to fit mechanistic signaling network models that provide insight into how cancer cells process information. Our dynamic single-cell-based models accurately predicted drug sensitivity and identified genomic features associated with drug sensitivity, including a missense mutation in DDIT3 predictive of PI3K-inhibition sensitivity. We observed similar trends in genotype-drug sensitivity associations in patient-derived xenograft mouse models. This work provides proof of principle that patient-specific single-cell measurements and modeling could inform effective precision medicine strategies.

INTRODUCTION

The aim of precision medicine is to use molecular markers of disease to enable tailored treatments. Currently, precision medicine is mainly informed by genomic and transcriptomic measurements, which are scalable and cost effective. For example, tumors with the *BCR-ABL* fusion are usually successfully treated with imatinib mesylate (Gleevec), breast cancer with *HER2* overexpression is treated with trastuzumab (Herceptin), and melanomas that express $BRAF^{V600E}$ are treated with vemurafenib (Zelboraf) (An et al., 2010; Garbe and Eigentler, 2018; Garrett and Arteaga, 2011). However, in treatment of breast cancer, patient-drug matching fails in a subset of patients, and, despite extensive characterization of genetic and epigenetic abnormalities in breast cancer, only a few targeted therapies are available (Coates et al., 2015; Cancer Genome Atlas Network, 2012; Nik-Zainal et al., 2016; Pereira et al., 2016). Even a well-established biomarker such as the amplification of *HER2* only partially predicts the tumor response: Only about half of all patients with *HER2*-amplified metastatic breast cancer respond to trastuzumab (Garrett and Arteaga, 2011).

Cancer cell lines are models for the human disease and can identify genomic features that correlate with and ultimately predict drug response (Barretina et al., 2012; Ghandi et al., 2019; Iorio et al., 2016; Neve et al., 2006). One aim of precision medicine is to identify and target the driver genomic alterations (Marcotte et al., 2016). Despite recent success in identifying driver alterations (Marcotte et al., 2016; Gholami et al., 2013), genomic

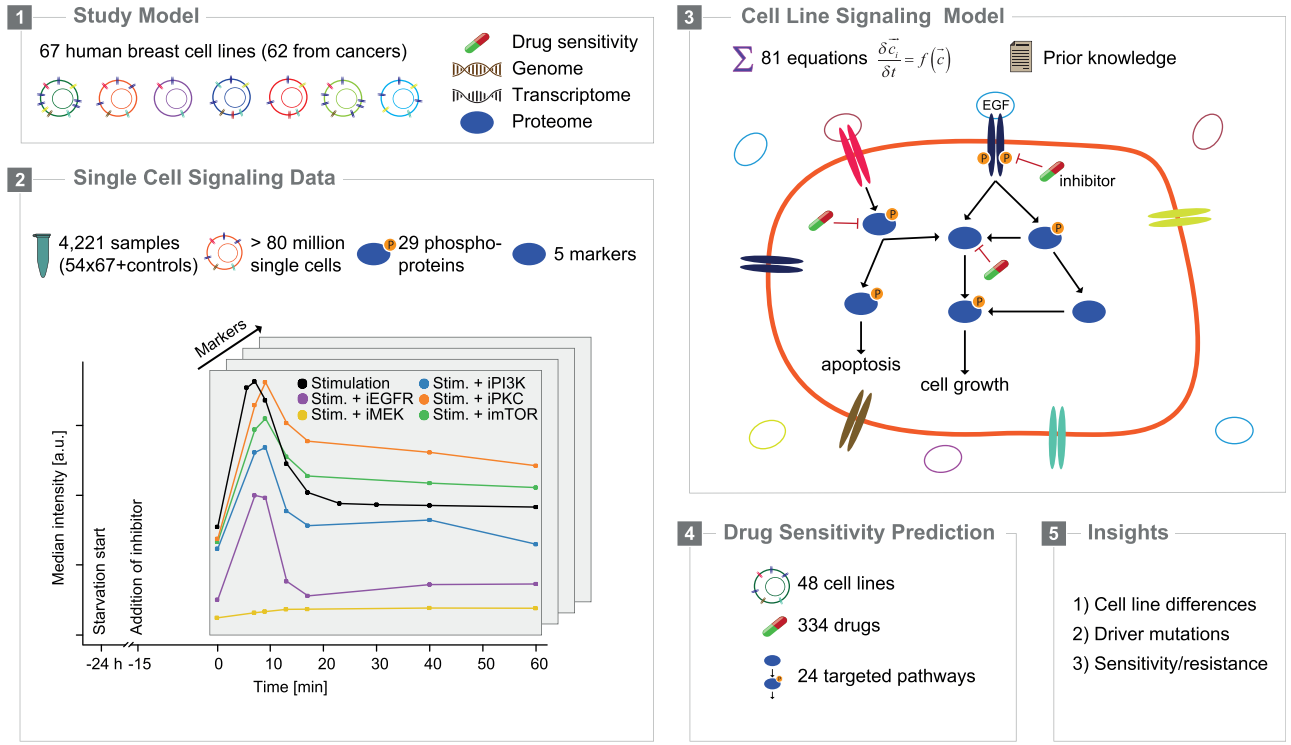

Figure 1. Experimental and computational approach to decipher the signaling landscape of breast cancer cell lines

information remains an incomplete predictor of drug sensitivity even in cell lines (Costello et al., 2014; Niepel et al., 2013). Genetic markers alone likely fail to predict drug response because genomic alterations have complex effects at the regulatory network and phenotypic level, and multiple drug resistance mechanisms at the level of signaling networks have been described (Lee et al., 2012; Yaffe, 2019). Phenotype-proximal readouts such as protein levels and post-translational modifications, which better reflect the status of the cell, are potentially better predictors of drug sensitivity than genomic sequence (Barrette et al., 2018; Beal et al., 2019; Fey et al., 2015; Fröhlich et al., 2018), especially when characterizing the response to a perturbation (Eduati et al., 2017; Hass et al., 2017; Meric-Bernstam et al., 2012; Niepel et al., 2013).

Many genetic and epigenetic alterations that drive cancer progression map to signaling pathways that control the key processes of growth, division, death, fate, metabolism, and motility (Forbes et al., 2011). Indeed, kinases and phosphatases involved in cellular signaling are the targets of some of the most effective anti-cancer therapeutics (e.g., HER2, EGFR, and RAF) and some of the most promising future targets as well (e.g., PKC, p38, and PI3K). However, the complex and redundant nature of the signaling network renders prediction of the effects of genomic alterations on the signaling state and drug sensitivity non-trivial. Furthermore, single-cell heterogeneity has been linked to fractional killing and drug resistance (Cooper and Bakal, 2017; Miura et al., 2018).

To develop a system to predict drug sensitivity, we used mass cytometry to map the single-cell signaling landscape of 62 breast cancer cell lines and five lines developed from healthy tissue. We quantified 34 markers over a 60-min stimulation with the growth factor EGF in the presence or absence of five different kinase inhibitors. The generated dataset revealed considerable heterogeneity in cellular signaling responses at both the population and single-cell levels. Based on these multiparametric mass cytometric measurements, we built cell-line-specific signaling network models. Predictors derived from these cell-line-specific models outperformed the state-of-the-art predictor based on transcriptomics data, for PI3K-MTOR-targeting drugs. Finally, we identified genomic aberrations predictive of drug response that were not identified without the signaling models. The associations of genomic variants with drug sensitivity identified by our signaling model were validated in patient-derived xenograft mouse models. Our analyses provide mechanistic insights into drug sensitivity and resistance mechanisms and suggest novel opportunities for patient stratification and combinatorial therapy.

RESULTS

The proteomes of breast cancer and normal breast cell lines

Since signaling networks are complex systems that can exhibit emergent properties, dynamic measurements under multiple conditions are required to model them effectively. As response to perturbation is known to be heterogeneous at the single-cell level and this heterogeneity is linked to drug resistance (Cooper and Bakal, 2017; Miura et al., 2018), we applied mass cytometry, using 35 antibodies (Table S1), to measure single-cell responses to EGF stimulation in the presence or absence of kinase inhibitors over a 10-point, 60-min time course (Figure 1; Table S2).

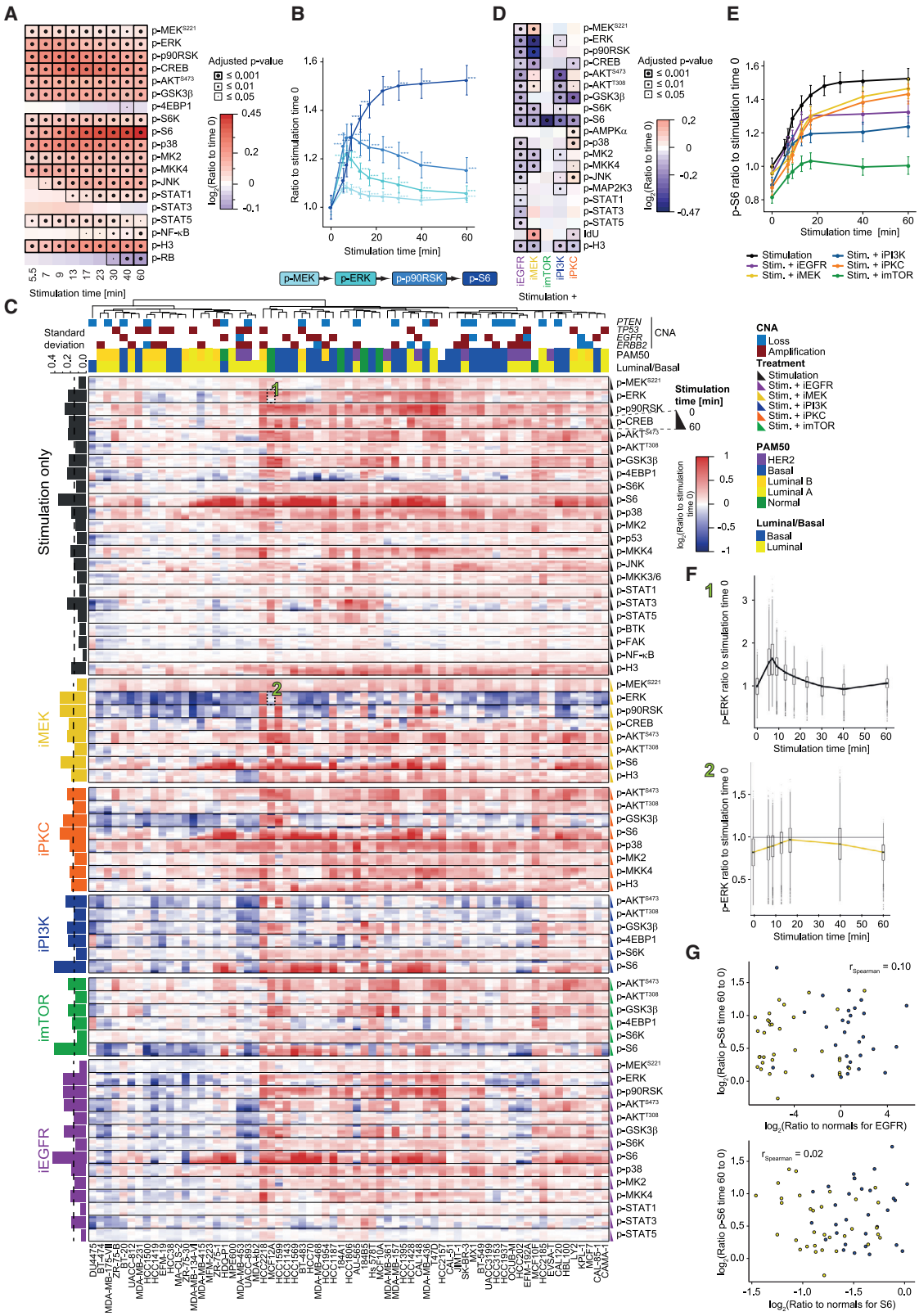

Figure 2. The signaling landscape of breast cancer cell lines

(A) Median intensity ratios of markers to time point zero for markers with significant differences over time in response to stimulation with EGF when responses of the 67 cell lines are averaged. Adjusted p values relative to time zero are represented by the dot size and the box thickness.

(legend continued on next page)

The kinase inhibitors selected target key signaling nodes and are well characterized and widely used: CI-1040 was the first MEK inhibitor to begin clinical development, pictilisib is a pan-PI3K inhibitor, rapamycin selectively inhibits mTOR, lapatinib inhibits both EGFR and HER2, and enzastaurin inhibits PKC (Allen et al., 2003; Folkes et al., 2008; Graff et al., 2005; Li et al., 2014; Xia et al., 2002) (Table S3). The resulting perturbation dataset includes quantitative information on 29 phosphorylation events covering the major signaling pathways, total protein abundance, DNA synthesis, and protein cleavage.

We characterized the signaling landscapes of a panel of human breast cancer cell lines and cell lines from healthy breast tissue (Marcotte et al., 2016) (Tables S4 and S5). The panel includes 62 cell lines generated from human breast tumors; 30 of these cell lines are basal-like and 32 are luminal-like, of which nine are known to overexpress HER2. These cell lines reflect some of the heterogeneity found in patient tumors, and both transcriptomic and genomic data, including data on single-nucleotide polymorphisms (SNPs) and copy-number aberrations (CNAs), are available for each line (Heiser et al., 2012; Marcotte et al., 2016; Neve et al., 2006). Importantly, for 48 of these cell lines, sensitivities (IC_{50} values) to 334 drugs have been measured (Picco et al., 2019; Yang et al., 2013). In total, we analyzed 4,000 samples and more than 80 million single cells (Figure 1), making it the most comprehensive signaling response dataset to date.

Since there has been no systematic characterization of protein abundances for these cell lines, we first conducted a quantitative proteomic analysis of all the cell lines using data-independent acquisition mass spectrometry. We quantitatively detected 9,031 proteins in cell lines grown without EGF stimulation. The proteomes of the five immortalized cell lines derived from normal tissue (184A1, 184B5, MCF10A, MCF10F, and MCF12A) were very similar to each other (mean Pearson's correlation coefficient for normal lines r = 0.94, across all lines r = 0.87) and clustered together (Figure S1A). The good quantitative accuracy of the data is exemplified by the high correlation between levels of Ku70 and Ku80 in all cell lines (Figure S1B); this is expected since levels of these two proteins are tightly controlled (Feng and Chen, 2012; Guo et al., 2019). Most detected proteins (7,328 proteins, 81%) were differentially abundant in at least one tumor cell line in comparison to the levels in the normal lines (Figure S1C). On an average, 2,600 proteins were differentially abundant when individual cancer cell lines were compared with the normal proteome; luminal cell lines had significantly more differentially expressed proteins than basal lines had (Figure S1D). In agreement with previous reports (Pozniak et al., 2016; Tyanova et al., 2016; Yanovich et al., 2018), the proteomes of luminal and basal cell lines mostly clustered together within each group, and the separation between the two groups was mostly driven by the differential expression of proteins involved in metabolic processes and other known proteins such as FOXA1, Vimentin, CD44, HER2, MET, and EGFR (Figures S1C, S1E, and S1F). The proteins that were differentially expressed between tumor and normal cell lines were enriched for breast-cancer-associated proteins and for GO terms linked to cellular signaling (Figures S1C and S1G), in agreement with prior knowledge that misregulated signaling plays an important role in cancer (Sanchez-Vega et al., 2018; Yaffe, 2019).

The signaling landscape of breast cancer cell lines

After analyzing static bulk proteomes of the cell lines, we exploited the dynamic single-cell data after EGF stimulation in order to examine the signaling responses by averaging phosphoprotein levels across cells. Twenty-one of the measured markers significantly changed over time (ANOVA, adj. p value ≤ 0.05). p-MEK^{S221}, p-ERK, p-AKT^{S473}, and p-S6 responded as expected (Figure 2A) (Klinger et al., 2013; Pennock and Wang, 2003). A detailed examination of ERK-MAPK pathway markers revealed delayed peak times and signal amplification for proteins progressively more distal from the stimulus (Figure 2B). Although abundances of most phosphorylated proteins increased upon stimulation, p-RB and p-4EBP1 levels decreased (Figure 2A).

In individual cell lines, there were considerable differences in fold changes of all 34 measured markers upon EGF stimulation (Figure 2C). Most cell lines responded strongly to EGF stimulation, but some did not respond at all and some even had lower levels of phosphorylation upon EGF stimulation (DU4475, BT-474, ZR-75-B, and MDA-MB-175-VII cells). These differences were not due to differences in initial levels of phosphorylation (Figure S2A). Overall, p-NF-κB varied the least, and p-S6 and p-4EBP1 varied the most. Depending on the cell line, p-4EBP1 increased (HCC2218, MCF12A, and HCC1599 cells) or decreased (MDA-MB-468, HCC1954, and HCC1187 cells). In

(B) Ratio of signal at stimulation time versus signal at time zero for indicated markers averaged over the 67 cell lines. The schematic depicts how signal is transmitted through the pathway. The error bars represent the standard error, and the asterisks the adjusted p values (*p $\leq$ 0.05, **p $\leq$ 0.01, ***p $\leq$ 0.001).
(C) Ratios of marker abundance at a given time point compared with time zero, ordered by increasing stimulation time, marker, and treatment, in all 67 cell lines clustered based on their signaling signature. CNA calling for *PTEN*, *TP53*, *EGFR*, and *ERBB2*, as well as PAM50 tumor subtype classifications and luminal/basal classifications are overlaid. Data are from two independent experiments combined by linear interpolation. The bar graph to the left of heatmap shows marker standard deviations across cell lines; the dotted line shows the treatment average. The single-cell data underlying the regions numbered 1 and 2 are shown in (F).
(D) Median intensity ratios of markers significantly altered by the indicated kinase inhibitors compared with EGF stimulation alone. Adjusted p values relative to time zero are represented by the dot size and the box thickness.
(E) Ratios of phospho-S6 signal at the indicated EGF stimulation time versus signal at time zero averaged over the 67 cells lines in the presence of the indicated kinase inhibitors. The error bars represent the standard error.
(F) Values for (1) p-ERK signal in MCF12A cells upon EGF stimulation and (2) p-ERK signal in MCF12A cells upon EGF stimulation in the presence of the MEK inhibitor normalized to the average signal at time point zero and plotted against time. Note that the time courses performed in the presence of inhibitors contain only a subset of the time points measured in absence of the inhibitors (Table S2). The medians correspond to those in the heatmap shown in (C) and are indicated by thick lines. The 25% and 75% quantiles are indicated by the boxes. The whiskers extend between the median and ± (1.58 × inter-quantile range). Values beyond the whiskers are plotted individually.
(G) Values of EGFR and S6 abundance (as $\log_2$ fold change) plotted versus p-S6 (as $\log_2$ time 0 to time 60 min after stimulation) for all cancer cell lines. Each dot represents one cell line, and the color refers to the basal/luminal classification (blue/yellow). The Spearman correlations are reported.

many cell lines there was no change in p-S6, but in 16 cell lines there was at least a 2-fold increase. Furthermore, phosphorylation of the STATs was highly cell line specific. Much of the inter-cell line heterogeneity was correlated. For example, p-ERK and p-p90RSK levels were correlated as were the two AKT phosphorylations, presumably due to common regulatory mechanisms. However, in certain cell lines this was not the case, hinting at differential regulatory mechanisms (Figures S2B and S2C). Signaling dynamics varied between cell lines as well. In most lines, p-ERK peaked at 9 min and then decreased (Figure 2B), but in some lines it had very different dynamics. For example, in T47D cells, levels plateaued at 9 min. Similar heterogeneity was observed for p-AKT^{S473}, p-p90RSK, p-S6, and p-MKK4.

When the responses of all 67 cell lines were averaged, most of the measured markers changed significantly upon treatment with at least one of five kinase inhibitors when compared with EGF stimulation alone (20 markers, Figure 2D). We observed an overall decrease in phosphorylation upon kinase inhibition, although certain markers increased, and all the inhibitors had the expected effects. For example, inhibition of EGFR resulted in reduced phosphorylation in the STAT, ERK-MAPK (p-MEK^{S221}, p-ERK, p-p90RSK, and p-CREB), and PI3K-AKT (both p-AKT sites, p-GSK3β, p-S6K, and p-S6) pathways. Notably, both levels and dynamics of the known signal integrator S6 changed significantly upon inhibition of all five pathways (Figures 2D and 2E). Analyses of average responses showed some intriguing behaviors. For instance, MEK inhibition induced an increase in levels of p-AKT but a decrease in p-S6K. Inhibition of PKC resulted in higher phosphorylation levels of several markers, including p-AMPKα, p-p38, and p-AKT^{T308}, possibly due to the release of the PKC-mediated inhibition of the kinase GSK3β.

There was more heterogeneity between cell lines upon perturbation with kinase inhibitors than with EGF stimulation alone (Figure 2C): the average standard deviation of the median fold change was significantly higher at 60 min upon treatment with all inhibitors than with EGF stimulation alone (ANOVA, adjusted p value = 0.026). In some lines, the expected targets of inhibitors did not respond. Among the most interesting cases were cell lines in which ERK phosphorylation was observed despite the presence of the MEK inhibitor (e.g., T47D, HCC2218, HCC1599, and CAL148 cells), GSK3β inhibition was observed although a PKC inhibitor was present (MCF12A, HCC2185, and MCF10F cells), and p-AKT^{S473} phosphorylation was observed despite PIK3 inhibition (HCC2118 and HCC1599 cells). In another example, inhibition of mTOR strongly diminished phosphorylation of S6 in most cell lines at 60 min (mean decrease of 1.65-fold) but did not in MCF10F and HCC2185 cells (Figures 2C and 2E). Overall, inhibition of EGFR resulted in the most unexpected behaviors in individual cell lines: We observed strong EGFR-dependent phosphorylation of S6 in MDA-kb2 cells and EGFR-independent phosphorylation of STAT3 and p90RSK in 184B5 and HCC202 cells, respectively. These phenotypes might be the result of either acquired resistance to the inhibitor or compensatory mechanisms.

When single cells from individual cell lines were evaluated, we generally observed homogeneous responses to perturbations, and bimodal responses were rare. Cellular variability (quantified as the coefficient of variation of the different marker levels) decreased with EGF stimulation time but increased upon kinase inhibition (Figures S2D and S2E). This phenomenon was apparent, for example, for p-ERK in MCF12A cells (Figure 2F). There were differences among the cell lines, however. For instance, whereas p-S6 cellular variability typically decreased over time post EGF addition, this did not hold true for HCC1500 cells (Figure S2F). Furthermore, the cell line-specific responses did not correlate directly with any tested genomic aberrations (e.g., with CNA status for *PTEN*, *TP53*, *ERBB2*, and *EGFR*, Figure 2C) or with the basal levels of major signaling proteins (Figure 2G). In summary, some signaling patterns are clearly conserved across cell lines, but there were no two cell lines where the responses to inhibition were the same, revealing the complexity of the signaling landscape in breast cancer cell lines.

Cell-line-specific signaling network models

Next, we used the generated data to train cell-line-specific mechanistic signaling network models as a step toward understanding the signaling landscape of breast cancer cell lines. We began with the markers targeted by our antibody panel, expanded and connected the network using prior knowledge available in Omnipath (Türei et al., 2016) (Table S6; Figure S3A), and built a dynamic mechanistic model using logic-based ordinary differential equations (Figure S3B). For the cell-line-specific signaling network models, we fit a node-specific speed factor (τ) that describes how rapidly the signal is relayed to that node via all upstream edges and an edge-specific transmission parameter ($\kappa_{A,B}$) that non-linearly describes how much of the signal is relayed from node A to node B (Figure 3A). Multiple steps are condensed into each of these parameters to increase scalability and to efficiently model multiple pathways together, which is required to use the complete set of markers. As a consequence, neither τ nor $\kappa_{A,B}$ are directly interpretable in a biochemical sense; however, they provide measures of pathway activity. For example, a small node-specific speed factor τ cannot be interpreted as describing an enzyme with slow kinetics but would be expected for nodes with slow or minimal responses to a perturbation.

We tested the fits of models to the data using the root mean square error (RMSE) (Hengenius et al., 2014). The models fit the data very well with an average error of only 5%, which is in the same range as biological replicate average error of 4% (Figure 3B). A few markers in some cell lines showed considerable error (0.3% of the marker and cell line combinations have a RMSE >15%, and 5% have RMSE >10%, e.g., 20% for p-S6K in AU565 cells and 17% for p-S6 in MPE600 cells), likely because the prior knowledge network is incomplete. Importantly, a single model for all cell lines performed poorly (data not shown), probably because it does not account for the observed heterogeneity between cell lines. The models captured both dynamics and inhibitor effects, as exemplified by the model for BT483 cells: The model accurately describes p-p90RSK time-dependent response to stimulation as well as its MEK-dependence (Figure 3C). Clustering of the cell lines based on τ and κ partly recapitulated the major clusters obtained based on the response to stimulation (Figures 2E and S3C). This suggests that our models—with only 107 model parameters—recapitulate the underlying 1,995 median points of information (markers × time points × treatments) in a condensed manner.

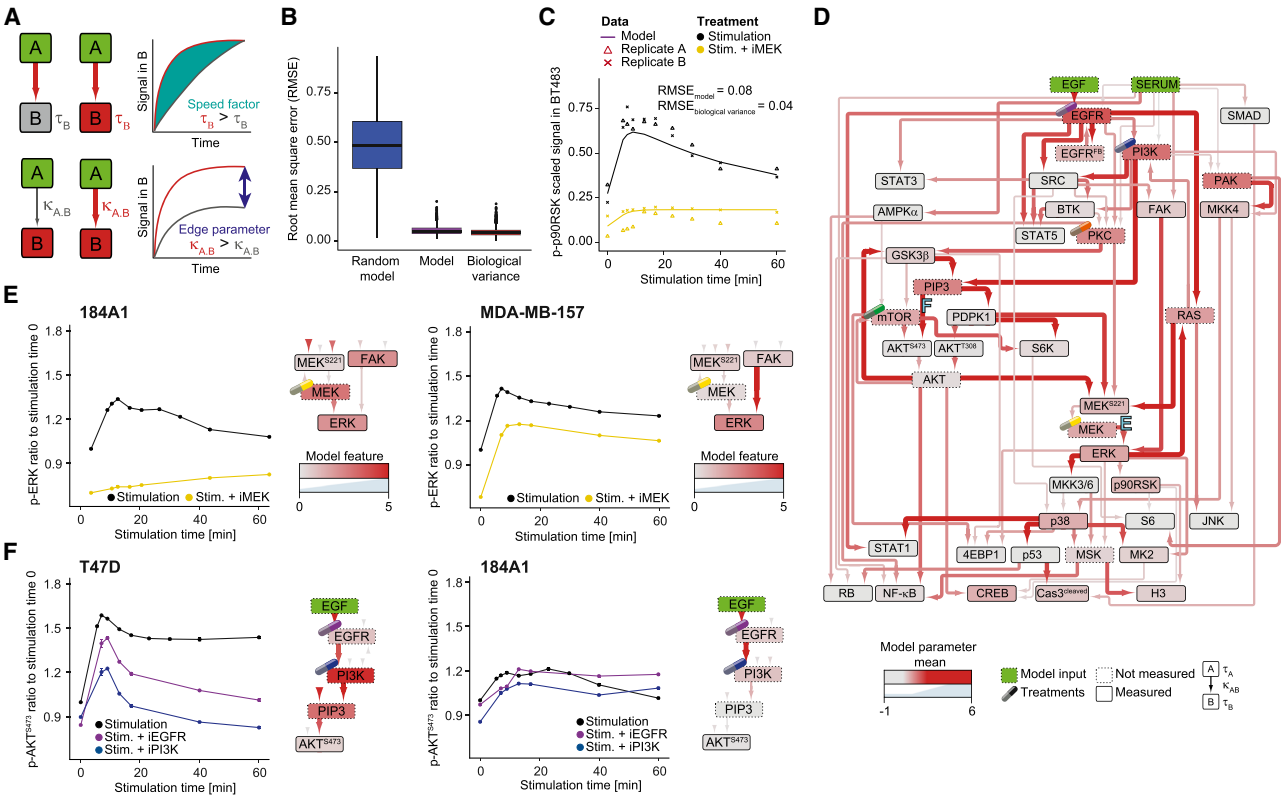

Figure 3. Cell-line-specific signaling models

(A) Illustrations of the effects of τ (speed parameter, top) and κ (edge parameter, bottom) on signal strength and dynamics in node B. The value of node A (input) changes over time from 0 to 1, and the signal of B is plotted as a function of time in the different modeled contexts depicted in the schematic.

(B) Marker and cell line RMSE of a random model, the cell-line-specific models, and the biological variance. The biological variance was computed as the average RMSEs between the medians and the two biological replicates for each marker and cell line. The thick lines indicate the median; the boxes and whiskers represent the 25% and 75% quantiles and the medians ± (1.58 × inter-quantile range), respectively. Data beyond the whiskers are plotted as dots.

(C) Representative fit for the 85th percentile of the RMSE for the p-p90RSK signal upon stimulation with EGF without (black) and with MEK inhibition (yellow) in BT483 cells. The scaled signals for the biological replicates A and B are plotted as triangles and crosses, respectively. The fitted model is plotted as a continuous line.

(D) The mean values for κ and τ of the mechanistic signaling network models for all 67 cell lines are represented as a signaling network. The color and thicknesses of edges indicate κ parameter values on a low-to-high scale (gray-red, thin-thick) and the node colors indicate τ parameter values on a low-to-high scale (gray-red). Modeled but not measured nodes are represented by dotted boxes, the model inputs are green, and intervention points are marked by an image of a drug capsule.

(E) p-ERK signal over an EGF stimulation time course for 184A1 cells (left) and MDA-MB-157 cells (right) under the indicated conditions. The ratios of median signal to signal at time point zero are plotted. Error bars are standard errors of the median of single cells. The schematics in each plot show excerpts from the cell-line-specific signaling model, represented as in (D).

(F) p-AKT^{S473} signal over an EGF stimulation time course for T47D cells (left) and 184A1 cells (right) under the indicated conditions. The ratios of median signal to that at time point zero are plotted. Error bars are the standard errors of the median of single cells. The schematics show relevant excerpts from the cell-line-specific signaling model, depicted as in (D).

The average network across all cell lines, although not informative about cell-line heterogeneity, provides a compact view of how breast cancer cells process information (Figure 3D). The most active pathways (as assessed by phosphorylation levels) have large signal transmission parameters. The highest κ was for the GSK3β·PIP3 edge (mean 3.14); this connection was one of the most consistently active across cell lines as it had the smallest coefficient of variation (CV = 67%, Figure S3D). Other very active connections were PI3K·PIP3, EGF·EGFR, AKT·MEK^{S221}, PIP3·AKT^{S473}, p38·STAT1, ERK·MKK3, and ERK·MKK6. Furthermore, under the studied conditions, the activation of p38, S6, and CREB occurred mostly independently from their known activators MKK3, MKK6, and p90RSK (Figure 3D), respectively (Remy et al., 2010; Roux et al., 2007; Xing et al., 1996).

The node-specific speed parameter τ is an indicator of reaction dynamics. Among the nodes with rapid dynamics in most cell lines were EGFR, PI3K, PIP3, PAK, and PKC (Figure 3D). In contrast, SMAD2, SMAD3, AMPKα, the STATs, SRC, MKK3, MKK6, and p53 nodes generally had slow dynamics (Figure 3D). The parameter τ is highly cell line dependent: The mean CV is 164%. The most conserved τ was that for the PI3K with a CV of 103% (Figure S3D). The parameters weakly correlated across cell lines (Pearson's correlation, r = 0.17, Figure S3E), reflecting the heterogeneous signaling landscape. Models of some cell lines were more correlated, indicative of quite similar dynamics

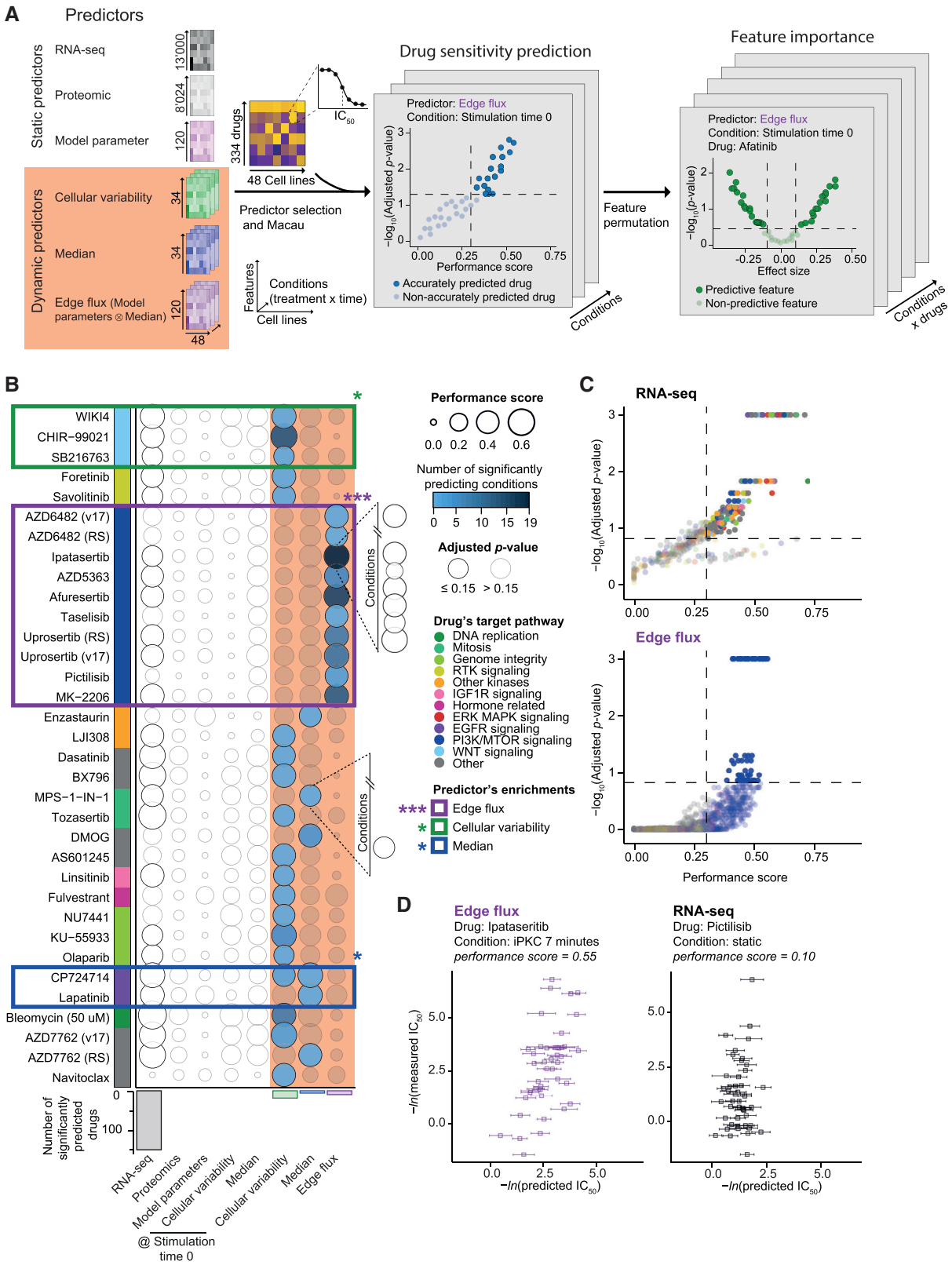

(legend on next page)

(r = 0.61 for HCC1428 and MDA-MB-362 cells), whereas others were very different (r = −0.15 for HCC1599 and EFM-192A cells, Figure S3E).

We next investigated the differences in signaling behavior between the luminal and basal cell lines, since this separation is well established and has clinical consequences. In accordance with the literature (De Andrade et al., 2016), we found higher EGFR expression (Figure S1F) and increased EGFR activation (SERUM·EGFR) in basal compared with luminal cell lines (Figure S4). STAT1 activation (p38·STAT1) was higher in luminal cell lines than in basal lines, as previously reported (Choi et al., 2013). Both p38 and ERK signaling were overall higher in luminal cell lines, although we noted overall higher activity in the PI3K pathway in basal cell lines. Although this was unexpected, it might be due to the known higher baseline activation of PI3K signaling in luminal cell lines, and hence a lower response to EGF or serum stimulus, which are captured as relative responses in our networks.

Since MEK is a clinical target of many drugs and MEK-independent ERK activation is a known resistance mechanism (Grimaldi et al., 2017; Kim and Giaccone, 2018; Lun et al., 2019; Simard et al., 2015), we examined MEK pathway activity. This pathway was active in most cell lines, but not in all. For example, in 184A1 cells, ERK activation was mostly MEK dependent, whereas in MDA-MB-157 cells it was mostly FAK dependent (Figure 3E). Our data are in line with previous reports that show that MDA-MB-157 cells are relatively resistant to BRAF-targeted drugs (PLX-4720 and dabrafenib) in comparison with the other cell lines (Picco et al., 2019; Yang et al., 2013). Cell-line-specific differences were also observed in the generally active PI3K pathway: In T47D cells, the phosphorylation of AKT^{S473} depended strongly on PI3K, whereas in 184A1 cells the dependency was less pronounced (Figure 3F). This is consistent with the fact that T47D cells are sensitive to PI3K inhibition (Picco et al., 2019; Yang et al., 2013). These cell-line-specific differences could be indicative of opportunities for intervention or patient stratification.

Prediction of drug sensitivity using dynamic predictors

We used the Genomics of Drug Sensitivity in Cancer (GDSC) dataset, which includes IC_{50} values for 334 drugs in 48 of the cell lines in our panel (Picco et al., 2019; Yang et al., 2013), to assess whether our dynamic models accurately predicted drug sensitivity. We used machine learning to predict the IC_{50} values using either static or dynamic predictors (Figure 4A). The static predictors, describing the steady state and acquired in absence of perturbation, included protein abundance measurements (log_2 fold change to the normal), RNA-seq data, and the non-linear logic-based model described in the previous section, parametrized by the τ and κ model parameters. Since the τ and κ parameters of the cell-line-specific logic signaling network models are time and treatment independent, these parameters do not provide direct information on which pathways are active in specific conditions or on the covariance over time and are thus considered as static. The dynamic predictors, describing the perturbed state, include 46 interdependent matrices, one for each individual combination of treatment and time point (Table S2), and include the median marker expression, the variability of marker expression at the single-cell level, and the edge flux. The edge flux represents the activity transferred between a node pair, similar to a metabolic flux, and capture the information transfer through the network and ultimately is important in defining a specific cellular state. Edge flux was computed from the model parameters (τ and κ). For example, in a kinase cascade A->B->C, the edge flux between A and B represents the increased activity per unit time of B caused by A. The edge flux depends on the activity of A (at time t) and on the strength of the edge (κ). Edge flux represents activity rather than phosphorylation even in the case of a kinase cascade, since phosphorylation of a site may sometimes inhibit the activity of the protein as $GSK3\beta^{S9}$ phosphorylation (Stambolic and Woodgett, 1994). The activity of a node is relative (1 means fully active and 0 means inactive) and the edge flux also has a value between 0 and 1 (see STAR Methods).

To predict drug sensitivity, we employed the Macau algorithm (Simm et al., 2017; Yang et al., 2018) (Figure 4A). We defined as a performance score the Pearson's correlation between predicted and measured IC_{50} (in a cross-validation scheme where predicted cell lines are not used for training) and identified significantly predicted drug sensitivity by requiring a false discovery rate (FDR) of less than 15% and a performance score greater than 0.3 as visualized on the volcano plot (Figures 4B and 4C). Based on these criteria, RNA levels (Marcotte et al., 2016) were predictive for the cell line sensitivity to 149 drugs (45% of all drugs tested). Variability of marker expression at the single-cell level, the edge flux, and median marker expression accurately predicted only 19, 9, and 6 drug sensitivities (Figure 4B). Use of protein abundance data, model parameters (τ, κ), or an RNA-seq dataset reduced to 34 dimensions with sparse principal component analysis (Erichson et al., 2020) predicted no sensitivities accurately (Figures 4B and S5A and data not

Figure 4. Prediction of drug sensitivity using dynamic predictors.

(A) Computational approach to predict drug sensitivity and identify predictive features.

(B) Upper: sensitivities that are predicted with significant accuracy by at least one dynamic predictor are shown (FDR 15% and performance score > 0.3, multiple hypothesis correction for the predicted drug measurements, n = 409) in rows versus the predictors in columns. Cellular variability and median were used as both static (stimulation time zero) and dynamic predictors, shown separately. The bubble color indicates the number of times the drug sensitivity was predicted with significant accuracy (for 46 combinations of treatment and time). The bubble size is proportional to the performance score of the best predictor. If the bubble circumference is light gray, sensitivity was not accurately predicted. Drugs are arranged by their target pathways (key to the far right); significantly predicted pathways are marked with a colored box and p values are shown at top right (*$p \leq 0.05$, **$p \leq 0.01$, ***$p \leq 0.001$; Fisher's exact test). Parentheses following the drug names give the version of the GDSC screen, if ambiguous. Lower: number of accurately predicted drugs per predictor is reported as a bar plot.

(C) Performance score plotted against the significance for predictions using the RNA-seq (top) and edge flux (bottom) predictors. Color code indicates putative target pathways. Thresholds for significance are indicated by dashed lines (FDR 15% and performance score > 0.3).

(D) Plots of measured and predicted IC_{50} values for the cell lines for which data are available from the GDSC dataset. Left: ipatasertib sensitivity was best predicted by the edge flux at 7-min stimulation in presence of the PKC inhibitor. Right: pictilisib sensitivity was not significantly predicted with RNA-seq data. The error bars represent the standard deviation from the 5-fold cross-validation.

shown). As expected, larger IC_{50} ranges and less missing data yielded more significant predictions (Figure S5B).

Whereas RNA-seq data accurately predicted sensitivities of more cell lines to drugs than other static inputs, there was no enrichment for drugs targeting specific pathways (Figure 4C). In contrast, the drug sensitivities accurately predicted by the dynamic predictors (edge flux, cellular variability, and median marker expression) were significantly enriched for drugs targeting parts of the modeled network (Fisher's exact test, Figure 4B). The edge flux most accurately predicted sensitivities of cell lines to drugs targeting the PI3K-MTOR signaling pathway (Figure 4C). For instance, sensitivities to ipatasertib and pictilisib were better predicted by the edge flux than by the RNA-seq-based model, and only the edge flux predicted sensitivities to pictilisib with significant accuracy (Figures 4D and S5C). In contrast, cellular variability and median marker expression were the most accurate predictors of sensitivities to drugs targeting the WNT and EGFR signaling pathways, respectively (Figure 4B).

For the 46 interdependent edge flux matrices, we plotted how many combinations of inhibitor treatment and time (i.e., conditions) were predictive of drug sensitivity (Figure 4B). In general, only a few conditions were predictive of sensitivity to a given drug (median of 1 condition per drug, Figure S5A). The edge flux was the most consistent predictor across conditions (median of 7 conditions per drug). For example, edge flux was a predictor of sensitivities to the AKT-targeting drugs ipatasertib and afuresertib. The median marker expression and cellular variability were also predictive of sensitivity to some drugs across conditions; however, these predictors were not accurate when only the stimulation condition was considered, demonstrating the importance of perturbation experiments (Figure S5A).

For different drugs, the predictors that were accurate differed. Sensitivities to just two drugs (CP724714 and AZD7762) of the 33 significantly predicted by the dynamic predictors were accurately predicted by two predictors (cellular variability and median marker expression), showing that the predictors provide orthogonal information (Figure 4B). For ten drugs (AS601245, AZD6482, DMOG, enzastaurin, fulvestrant, navitoclax, NU7441, pictilisib, and taselisib), sensitivities were accurately predicted only by the dynamic predictors. Importantly, the predictions recapitulate distinct drug sensitivity patterns for specific drugs in basal and luminal cell lines (Figure S5D). Thus, the characterization of the signaling landscape improved drug sensitivity prediction of selected kinase inhibitors.

Features affecting drug sensitivity predictions

We next identified the features, such as the median expression of a phosphorylated protein, that are important for the drug sensitivity prediction (Figure 4A). We extracted feature importance directly from the drug sensitivity models using a procedure similar to that used to retrieve loadings for linear models. We calculated an effect size per drug for each feature and computed the significance of each effect size (Figure 4A). The effect size is a measure of the contribution of a particular feature to the accurate drug sensitivity prediction, and as such may be useful for understanding drug sensitivity and resistance mechanisms. We note that effect sizes as defined here are not clinically interpretable. We defined features with positive effects as those higher in resistant cell lines and not in sensitive ones; features with negative effects were those higher in sensitive but not resistant cell lines.

Features that significantly contributed to overall accuracy of prediction of drug sensitivity and resistance (effect size > 0.01 or < -0.01 and 5% FDR, see STAR Methods) were identified by averaging across all models for all drugs (Figures 5A and S6A). The edge flux has more predictive features than other predictors (11 of the 15 most predictive features, Figure 5B). For example, three of the edges connecting PKC to the signaling network are among the 15 most predictive features, with the edge from BTK to PKC being the most predictive feature. The most predictive feature is the level of GAPDH. Whereas GAPDH median levels were predictive of drug sensitivity, its cellular variability was predictive of drug resistance. The opposing effects of median levels and cellular variability were also observed for other proteins such as Ki-67, p-MKK4, and p-MEKS221 (Figures S6A and S6B).

Next, we repeated the same analysis but instead of averaging across all drugs we averaged across groups of drugs targeting selected biological pathways (Figures 5C, S6C, and S6D). This approach minimized contributions of off-target effects and provided insights into drug-class-specific effects. Most features with a significant predictive effect were correlated with sensitivity (e.g., BTK·PKC) or resistance (e.g., p38·MK2) across all drug classes (Figures 5C, S6C, and S6D). We did, however, observe drug-class-specific patterns in which certain features are predictive only for drugs targeting a certain pathway (Figures 5C, S6C, and S6D). We also identified features that are sometimes predictive of sensitivity and sometimes of resistance, depending on the targeted pathway. For example, the AKT,RAS·MEKS221 edge flux (the parameter controlling MEK activation, which integrates both the positive influence of RAS and the negative influence of AKT) correlated with sensitivity to drugs targeting EGFR and PI3K-MTOR signaling and resistance to drugs targeting ERK-MAPK and IGF1R signaling (Figures 5C and 5D). Although not predictive for overall drug sensitivity or resistance, p90RSK correlated with sensitivity to drugs targeting several specific pathways (Figures 5A, 5C, S6A, S6C, and S6D): its activation through ERK (ERK·p90RSK) was predictive of sensitivity to ERK-MAPK-pathway-targeted drugs, p90RSK·S6 of sensitivity to drugs targeting EGFR signaling, and its cellular variability of resistance to ERK-MAPK signaling drugs (Figures 5D and S6E). In other examples, the cellular variability of p-STAT1 was particularly predictive for a subset of drugs that target PI3K-MTOR, and the median level of p-AMPKα was predictive of sensitivity to PI3K-MTOR inhibition (Figures 5D, S6C, S6D, and S6E). An interesting instance is the extent to which the cellular variability of the proliferation marker Ki-67 predicted resistance across drug classes (Figures 5D and S6E). Large Ki-67 variability was predictive of sensitivity to EGFR signaling drugs. Notably, cellular variability of Ki-67 was most predictive for drugs targeting DNA replication. This supports the ''proliferation rate paradox'': that is, the finding that many chemosensitive human cancers have low proliferation rates (Mitchison, 2012). The levels of Ki-67 are predictive for sensitivity, but the predictive power is smaller than that of the cellular variability (Figures S6B and S6E). Additional identified trends include the dependence on the source of activation (e.g., ERK, PI3K, and PKC, Figure 5A) opposing effects of some features on closely related pathways

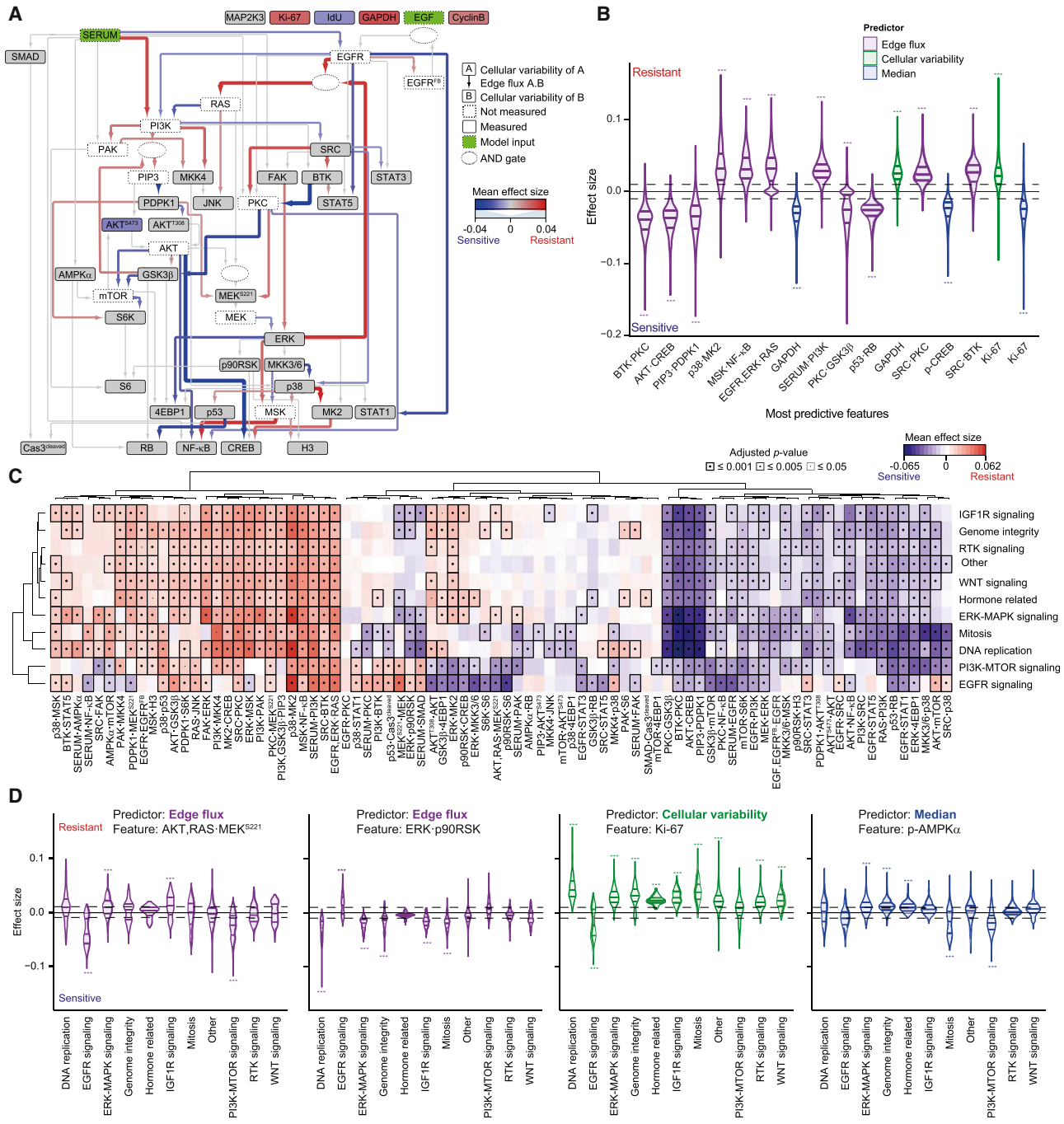

Figure 5. Features that influence drug sensitivity predictions

(A) Significant effect size features (contributing to the accurate drug sensitivity prediction) of the cellular variability (nodes) and edge flux (edges) predictors are represented on the signaling network. The colors represent the mean effect sizes over all conditions and drugs. The edge thicknesses are proportional to the absolute values of the mean effect sizes (FDR 1%, see STAR Methods).

(B) Effect size distributions for the most predictive 16 features across the three dynamic predictors. The horizontal lines represent the medians and the 25% and 75% quantiles. The color of the distribution indicates the predictor. The arbitrary large effect size threshold (0.01) is indicated by the dashed line. *p ≤ 0.05, **p ≤ 0.01, ***p ≤ 0.001.

(C) Mean pathway-specific effect size features of the edge flux with drugs binned according to the target pathway in rows and features shown in columns (FDR 5%). Both the features and target pathways were hierarchically clustered. Mean effect sizes are indicated on a low-to-high color scale. For each class the lowest adjusted p value of all side-by-side comparisons is indicated by the dot size and the box thickness. The group "other" contains all the drugs not falling into another group.

(D) Effect size distributions for four selected features showing pathway-specific effects. The selected predictors and features are indicated in each case. The significant threshold of 0.01 minimum effect size is plotted as a dashed line. The horizontal lines indicate the median and the 25% and 75% quantiles. AKT,RAS·MEK^{S221} represents the parameter controlling MEK activation and it integrates both positive RAS and negative AKT influence. *p ≤ 0.05, **p ≤ 0.01, ***p ≤ 0.001.

CellPress
OPEN ACCESS

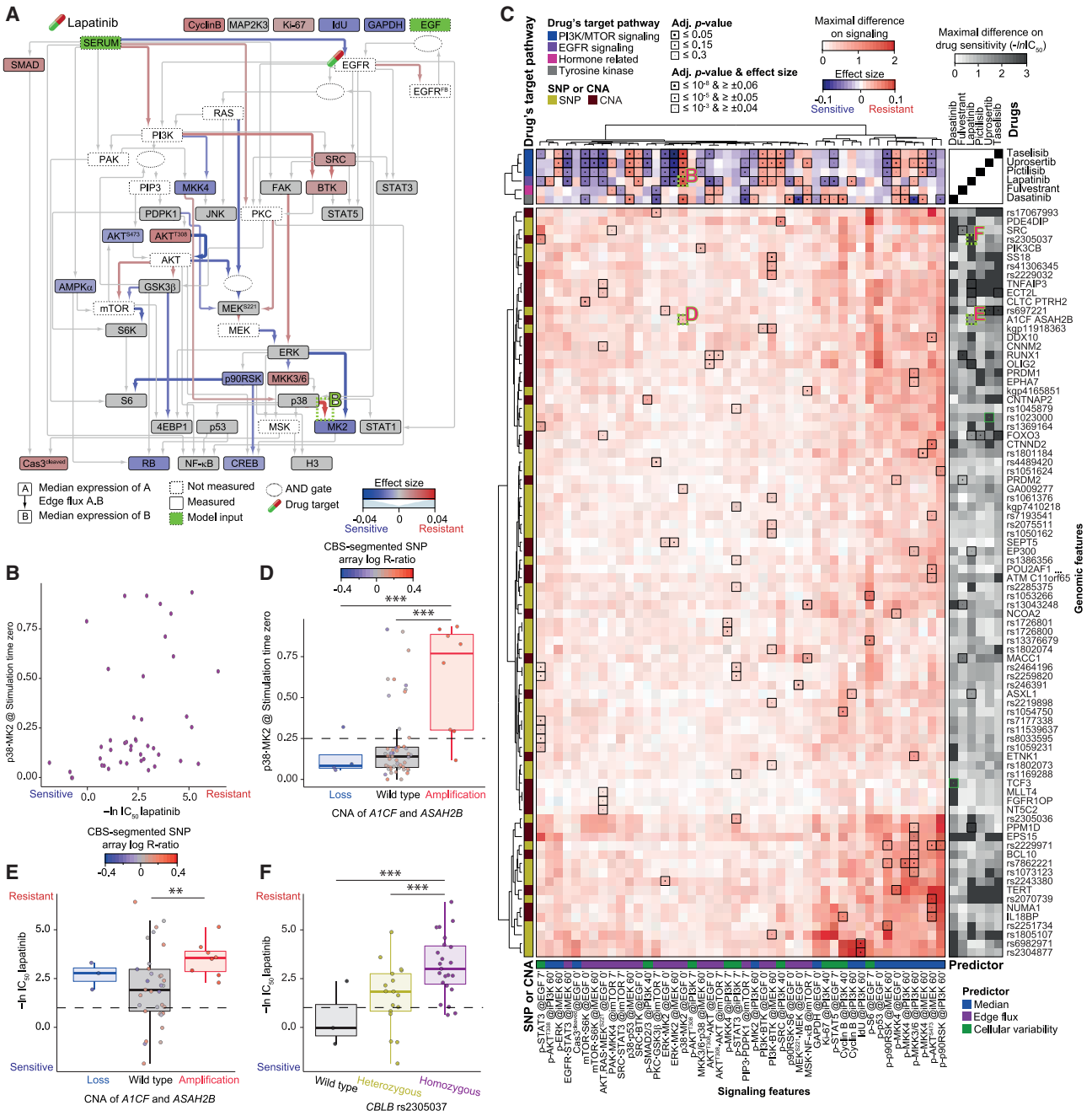

Figure 6. Resistance and sensitivity to lapatinib and genomic variants associated with drug sensitivity

(A) Significant effect-size features of the median (nodes) and edge flux (edges) predictors represented on the signaling network for lapatinib (FDR 15% and effect size > 0.01 or < −0.01). The effect sizes are indicated using color (nodes and edges), and the edge thicknesses are proportional to the absolute values of the effect sizes. An image of a drug capsule highlights the putative drug target. In each case the conditions with the highest performance scores are plotted: PI3K inhibitor 60 min and stimulation time zero for medians and edge fluxes, respectively. The data in region labeled B are shown in that panel.

(B) Values for the edge flux p38·MK2 (at stimulation time zero) plotted against lapatinib IC_{50} for different cell lines (n = 42). Each data point represents a cell line.

(C) Upper: heatmap of the effect size of the selected signaling features (columns) and the six selected drugs (rows) for 48 cell lines. The drug's target pathway and predictors are overlaid. The effect sizes are indicated on a low-to-high color scale. The adjusted p value and effect size thresholds are indicated by the dot size and the box thickness. Lower left: heatmap of the maximal difference in selected signaling features (columns) among genomic statuses (rows) in 64 and 61 cell lines for filtered CNA and SNP, respectively. Both the signaling features and the genomic features were hierarchically clustered. SNP or CNA status is overlaid. Only genomic features with at least one significant link resulting from the QTL analyses are reported, and the adjusted p values are indicated by the dot size and the box thickness. Lower right: heatmap of maximal differences in IC_{50} values (*–ln*) for dasatinib, fulvestrant, lapatinib, pictilisib, taselisib, and uprosertib (columns) among genomic statuses (rows) in 42 and 40 cell lines for CNAs and SNPs, respectively. The adjusted p value of the QTL analysis using the IC_{50} values directly and using an ANOVA on the genomic features identified through the signaling are indicated by the dot size and the box thickness in green and black, respectively. In

(legend continued on next page)

(e.g., ERK·p90RSK opposite effects on EGFR and ERK-MAPK signaling, Figure 5D). In sum, these findings confirm the utility of integrating dynamic perturbation data with mathematical modeling and show how identical signaling features can be predictive of sensitivity and resistance depending on the context.

Resistance and sensitivity to PI3K and EGFR inhibition

Finally, we used the dynamic predictors to probe mechanisms of drug resistance and sensitivity. We focused on inhibition of two clinically relevant targets, EGFR and PI3K, considered essential to basal and luminal breast cancers, respectively (Marcotte et al., 2016). The median marker expression after treatment with the PI3K inhibitor for 60 min predicted the sensitivities of cell lines to the FDA-approved lapatinib, an inhibitor of EGFR and HER2 used in combination therapy for HER2-positive breast cancer (Giampaglia et al., 2010), with significant accuracy (Figure 4B). We identified the features significantly predictive of lapatinib resistance or sensitivity for all dynamic predictors, since they all performed quite well in predicting lapatinib sensitivity (Figures 4B and S5A). Consistent with previous reports (Campbell et al., 2004; Zhang et al., 2011), alternative activation of PI3K (SERUM·PI3K, in contrast to EGF-dependent PI3K activation via EGFR·PI3K and RAS·PI3K) and SRC correlated with lapatinib resistance, and strong EGFR/HER2 activity (SERUM·EGFR, modeling the EGF-independent EGFR activation) correlated with sensitivity (Figure 6A). Strikingly, the median expression levels of one of the two phosphorylated forms of AKT correlated with lapatinib resistance and the other with sensitivity. The variabilities of p-STAT5 and p-STAT3 were more predictive of sensitivity than were the median levels of expression (Figures 6A and S6F); median expression of the phosphorylated forms of STAT5 and STAT3 were previously reported to be predictive of lapatinib, canertinib, and afatinib sensitivity (Gschwantler-Kaulich et al., 2016). Interestingly, p-MK2 median expression correlated with lapatinib sensitivity, and the p38·MK2 and ERK·MK2 edge fluxes strongly correlated with resistance and sensitivity, respectively (Figures 6A and 6B). These results are indicative of the importance of MK2 in the response of cells to lapatinib.

The edge flux was the only predictor that accurately identified cell lines sensitive to pictilisib, a pan-PI3K inhibitor (Figures 4B, 4D, and S5A). S6K activation by mTOR (mTOR·S6K), activation of STAT1 and STAT3 (EGFR·STAT3, SRC·STAT3, and EGFR·STAT1), and cellular variability of MKK4, p90RSK, and MKK3/6 were pictisilib sensitivity predictors, whereas induction of the oncogene-induced senescence pathway (p38·p53) was predictive of resistance (Figure S6G). ERK pathway activation and cellular variability of the phosphorylated STATs were predictive of sensitivity to pictilisib (Figure S6G), PI3K-MTOR inhibitors (Figures 5C, S6C, and S6D), and the PI3K-inhibitor taselisib (Figure S7A). Pictilisib-specific effects were also observed: cellular variabilities of p-p53 were predictive of sensitivity to pictilisib but not to taselisib or the PI3K-MTOR drug group and EGFR·PKC was only prominently predictive of resistance to pictilisib (Figures 5C, S6C, S6D, S6G, and S7A). Off-target effects or differences in targets or mechanism could explain such drug-specific characteristics, and these must be considered when designing clinical trials.

Using dynamic predictors, we were also able to predict sensitivities of drugs that do not directly target a protein present in our network, likely because these drugs indirectly affect the network. For example, cellular variability was the only predictor of response to fulvestrant (Figure 4B), a selective estrogen receptor degrader used to treat hormone-receptor-positive breast cancer (Nathan and Schmid, 2017). Estrogen signaling interplays with both the ERK-MAPK and the PI3K-MTOR signaling pathways (Tanos et al., 2012), which were monitored by the antibodies in our mass cytometry panel. An analysis of feature importance revealed that EGFR, SRC, and ERK play defining roles in the response to this drug (Figure S7B). Hence, our predictors can be used even when the abundances of direct targets are not quantified, as long as they are regulated through the signaling pathways that we model.

Signaling features identify genomic variants associated with drug sensitivity

The identification of genomic aberrations that correlate with drug response is an essential step toward personalized medicine. Identification of these aberrations is challenging, and the effect sizes often limited (Garnett et al., 2012; Menden et al., 2018). Indeed, a quantitative trait locus (QTL) analysis (Clément-Ziza et al., 2014) of sensitivities to dasatinib, fulvestrant, lapatinib, pictilisib, taselisib, and uprosertib identified only one CNA (TCF3 for dasatinib) and one SNP (FNBP1 (rs1023000) for uprosertib) associated with drug sensitivity (Figure 6C, green highlights on the lower right heatmap), in spite of restriction of the search space to the COSMIC list of oncogenes (736 SNPs and 518 CNAs in 706 oncogenes) (Sondka et al., 2018) and a 30% FDR threshold (Eduati et al., 2017). We speculated that we could take advantage of our signaling models to improve QTL performance. We ran QTL analyses on 46 signaling features predictive of sensitivity to dasatinib, fulvestrant, lapatinib, pictilisib, taselisib, and uprosertib (Table S7; Figure 6C). The analysis revealed associations between signaling features and 55 SNPs and 38 CNAs (Figure 6C). For instance, *A1CF/ASAH2B* CNA status was predictive of the lapatinib-predictive p38·MK2 edge flux (Figures 6C and 6D) and the rs2305037 SNP (in the *CBLB* gene) of p-STAT3 cellular variability (Figure S7C). Notably, although we did not identify any genomic aberrations linked to

both the lower left and right heatmaps, the maximal differences are indicated on a low-to-high color scale capped at two and three, respectively. The data in regions labeled B, D, E, and F are shown in those panels.

(D) Values of the edge flux p38·MK2 (at stimulation time zero) plotted against CNA status of *A1CF/ASAH2B* (n = 64 cell lines). Thick lines indicate medians, the dashed line indicates the arbitrary threshold for high activity, boxes indicate the 25% and 75% quantiles, and whiskers extend between the median and ± (1.58 × inter-quantile range). Each data point represents a cell line, and the color intensity indicates the amplification status on a low-to-high scale (blue-gray-red, ANOVA followed by Tukey honest significant differences computation: *p $\leq$ 0.3, **p $\leq$ 0.15, ***p $\leq$ 0.05).

(E) IC_{50} values (–*ln*) for lapatinib plotted against CNA status of *A1CF* and *ASAH2B* (n = 42 cell lines). Plots and statistical analysis are as in (D), except that the dashed line indicates the arbitrary threshold for sensitivity (1).

(F) IC_{50} values (–*ln*) for lapatinib plotted against SNP status of rs2305037 (*CBLB* gene, n = 40 cell lines). Plots and statistical analysis are as in (D), except that the dashed line indicates the arbitrary threshold for sensitivity (1) and that colors indicate the SNP status.

lapatinib sensitivity directly, inclusion of signaling features revealed that cell lines with amplification in *A1CF/ASAH2B* or those homozygous for rs2305037 were generally more resistant to lapatinib (Figures 6E and 6F). Furthermore, we identified ten genomic aberrations linked to the median expression levels of p-MKK3 and p-MKK6, which were, in turn, predictive of lapatinib resistance (Figure 6A). Two of these genomic aberrations (*EP330* and *PPM1D*) showed potential to differentiate the lapatinib response (Figure S7D). CNAs of *PRDM2* and *MACC1* were linked to fulvestrant sensitivity through their link to p-MKK4 median expression and the MSK·NF-κB edge flux, respectively (Figure S7E). Additionally, the ERK·MK2 edge flux was associated with the SNP rs697221 that causes a missense change in the sequence of the gene *DDIT3*. ERK·MK2 was predictive of sensitivity to all three PI3K targeted inhibitors studied (pictilisib, uproseritib, and taselisib). Overall, through our characterization of signaling, we identified 21 genomic aberrations predictive of drug sensitivity (none were identified for dasatinib, Figure 6C, black highlights on the lower right heatmap). Thus, a QTL analysis on the signaling phenotype can identify gene variants predictive of drug sensitivity even when genetic effects on drug sensitivity are too weak to be identified directly.

Since breast tumors are routinely clinically characterized for gene variants, we went on to validate the drug sensitivity associations with gene variants found through our modeling approach. We tested genomic associations with drug sensitivity in patient-derived tumor xenograft (PDTX) models of breast cancer, since these mouse models closely mimic characteristics of patient tumors (Bruna et al., 2016). We had overlapping data between our cell lines and PDTX models for pictilisib, taselisib, and lapatinib, including 32 PDTX mouse models with corresponding CNA information. After filtering for specific relationships coming from our signaling models (i.e., drug sensitivity for amplification versus loss or drug sensitivity for amplification versus wild type) with at least eight observations in each dataset, we found that six of the eight relationships had significant copy-number-dependent differences in drug sensitivity in the cell line dataset. The observed trends were in agreement between the *in vitro* (cell lines) and *in vivo* (PDTX models) in 87% of cases (Figures 7A–7E). The strongest trends (at a p value cutoff of either 0.2 or 0.5) found in the PDTX dataset were in agreement with our cell line data (n = 2 and 3, respectively). This strong agreement is notable considering the substantial biological variability between the cell line and PDTX models. Although the small number of comparisons, due to the limited availability of PDTX data, limits the generalizability of our findings, these results nevertheless strongly suggest the *in vivo* validity of the genotype-drug sensitivity associations identified using our signaling model. In order to probe whether such similarities in trends could have been obtained by chance, and to further assess whether our signaling models add value to the genotype-drug sensitivity association analysis, we conducted the same comparison between *in vitro* and *in vivo* systems for the top CNA-drug sensitivity associations that had been predicted by direct QTL. After applying the same filters, for the 30 relationships we could compare, the mouse PDTX data agreed with the trends in the *in vitro* data in only 47% of cases (Figures 7F and S7F–S7H). Further, only one of three strongest effects (p value < 0.5) in the *in vivo* data agreed with the *in vitro* trends. Thus, the agreement is weaker than in our model-derived associations. These results further strengthen our observations that our signaling model identifies biologically robust CNA-drug sensitivity associations.

DISCUSSION

We used mass cytometry to interrogate signaling in a panel of 62 breast cancer cell lines and five cell lines generated from normal tissue, to generate the largest multiplex single-cell signaling dataset to date. Although clustering of proteomic data from unstimulated cells accurately separated luminal and basal phenotypes, there was, unexpectedly, no clear separation between luminal and basal phenotypes upon clustering based on signaling parameters. This may reflect the targeted nature of our measurements or may indicate that there is actually a continuum of phenotypes rather than a clear luminal/basal separation. The logic-based signaling network models condense the signaling features enabling visualization and prediction of drug sensitivity/resistance. We were surprised to find that the model parameters did not predict the responses to drugs, whereas the edge flux did, in a manner mostly independent of the specific condition. This could be because the edge flux maintains the signaling correlation structure and integrates information about all conditions, such that its information content does not change with time or treatment as drastically as for the other predictors. It was not surprising that the edge flux was not highly predictive for all drugs, since most drugs target processes not monitored by our antibody panel. The predictive accuracy of the edge flux was similar to or better than RNA-seq, despite the almost 300-fold difference in the number of fitted features.

Using the edge flux, we were able to break down complex relationships between signaling and drug sensitivity. We showed that PKC, known to have complex functions in cancer progression (Garg et al., 2014), is among the most important hubs, governing both sensitivity and resistance to many drugs. PKC inputs (SERUM·PKC, EGFR·PKC, SRC·PKC, and BTK·SRC) were quite variable across cell lines, but downstream activity, as assessed by model parameters, was similar across cell lines. We also observed intriguing differential effects of ERK: its tumor suppressor activity was MEK dependent and involved 4EBP1 activation, whereas the tumor-promoting activity was FAK dependent and involved MSK1 and MSK2 activation.

Features correlating with sensitivity have potential in patient stratification. For example, cellular variability of p-STAT5 and p-STAT3 were predictive of lapatinib sensitivity and could therefore be used as a stratification marker. This is consistent with previous reports that inhibition of phosphorylation of JNK and STAT5 by lapatinib was observed only in sensitive cell lines (Gschwantler-Kaulich et al., 2016). *PI3K* mutational status is often not predictive of response to *PI3K*-targeted drugs (Krop et al., 2016; Schmid et al., 2016; Schöffski et al., 2018). The edge flux and the median marker expression in our data suggest important roles of p-MKK4 and p-STAT3 in defining pictilisib sensitivity; both have potential as markers for improving patient stratification.

Features correlating with resistance could aid in selection of efficacious combination therapies. Information on variability at the single-cell level allowed us to predict susceptibility to navitoclax, fulvestrant, NU7441, and AS601245, drugs for which other

A

p-value <= 0.5
p-value <= 0.2

		Cell lines			PDTX		
Drug	Gene	loss to *wt*	loss to gain	gain to *wt*	loss to *wt*	loss to gain	gain to *wt*
pictilisib	FOXO3	Resistance	Resistance	Sensitivity	Resistance	Resistance	Sensitivity
lapatinib	ASXL1			Resistance			Resistance
taselisib	ECT2L	Resistance			Resistance		
taselisib	FOXO3	Resistance	Resistance	Sensitivity	Resistance	Resistance	Resistance

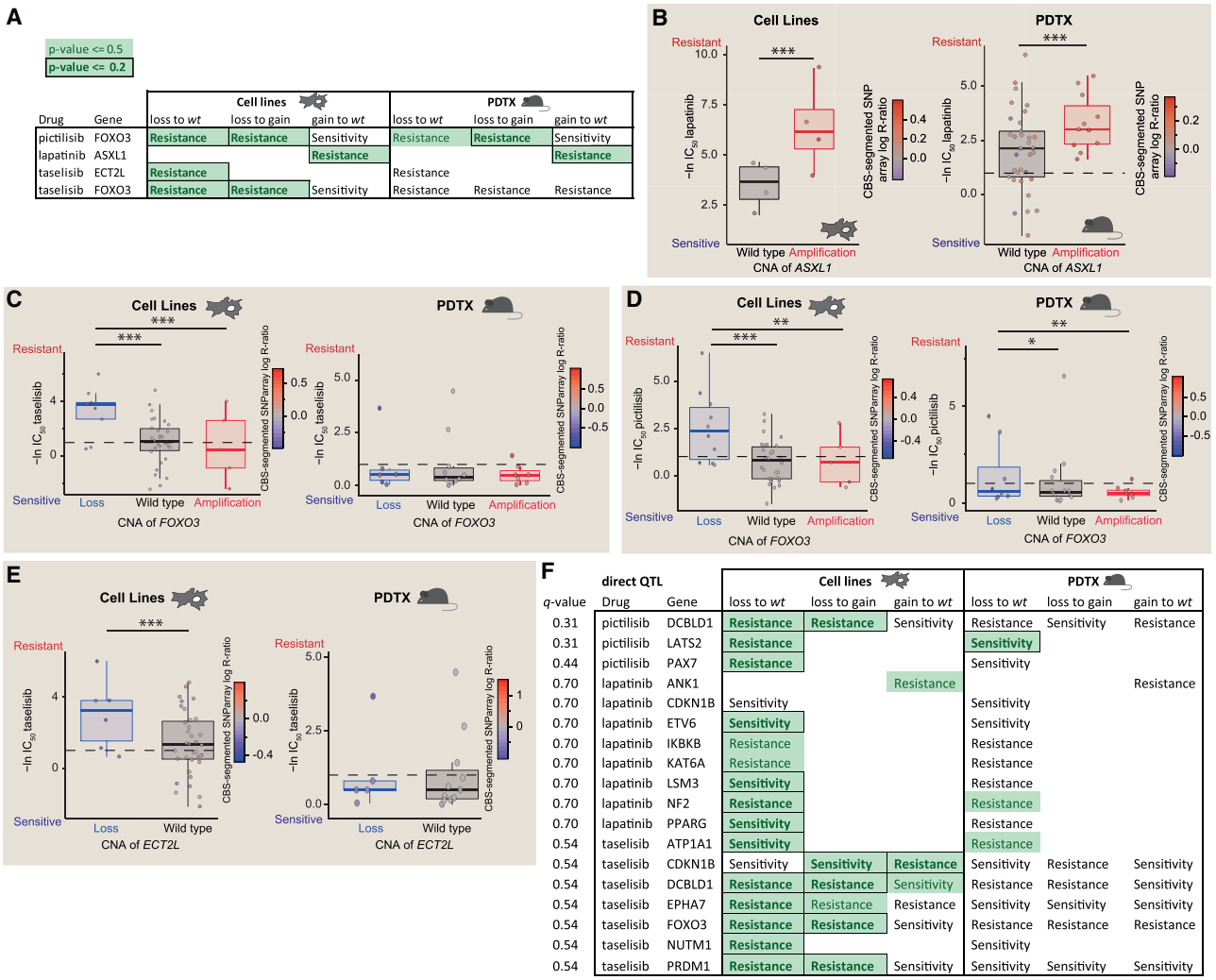

F

q-value	direct QTL Drug	Gene	Cell lines loss to *wt*	loss to gain	gain to *wt*	PDTX loss to *wt*	loss to gain	gain to *wt*
0.31	pictilisib	DCBLD1	Resistance	Resistance	Sensitivity	Resistance	Sensitivity	Resistance
0.31	pictilisib	LATS2	Resistance			Sensitivity		
0.44	pictilisib	PAX7	Resistance			Sensitivity		
0.70	lapatinib	ANK1			Resistance			Resistance
0.70	lapatinib	CDKN1B	Sensitivity			Sensitivity		
0.70	lapatinib	ETV6	Sensitivity			Sensitivity		
0.70	lapatinib	IKBKB	Resistance			Resistance		
0.70	lapatinib	KAT6A	Resistance			Resistance		
0.70	lapatinib	LSM3	Sensitivity			Resistance		
0.70	lapatinib	NF2	Resistance			Resistance		
0.70	lapatinib	PPARG	Sensitivity			Resistance		
0.54	taselisib	ATP1A1	Sensitivity			Resistance		
0.54	taselisib	CDKN1B	Sensitivity	Sensitivity	Resistance	Sensitivity	Resistance	Sensitivity
0.54	taselisib	DCBLD1	Resistance	Resistance	Sensitivity	Resistance	Resistance	Sensitivity
0.54	taselisib	EPHA7	Resistance	Resistance	Resistance	Sensitivity	Sensitivity	Sensitivity
0.54	taselisib	FOXO3	Resistance	Resistance	Sensitivity	Resistance	Resistance	Resistance
0.54	taselisib	NUTM1	Resistance			Sensitivity		
0.54	taselisib	PRDM1	Resistance	Resistance	Sensitivity	Sensitivity	Sensitivity	Sensitivity

Figure 7. Trends in drug sensitivity-CNA associations in cell line and PDTX data

(A) Trends in drug sensitivity-CNA associations predicted by our signaling model in cell line data and PDTX mice. Strong trends are highlighted in green and bold green based on a p values $\leq$ 0.5 and $\leq$ 0.2 (ANOVA followed by Tukey honest significant differences computation).

(B) IC_{50} values (–*ln*) for lapatinib plotted against CNA status of *ASXL1* (n = 42 cell lines and 11 PDTX mouse). The dashed line indicates the arbitrary threshold for sensitivity (1). *In vitro* data (cell lines) are on the left and *in vivo* data (PDTX) on the right. Thick lines indicate medians, boxes indicate the 25% and 75% quantiles, whiskers extend between the median and ± (1.58 × inter-quantile range). Each data point represents a cell line or mouse model, and the color intensity indicates the amplification status on a low-to-high scale (blue-gray-red, ANOVA: *p $\leq$ 0.5, **p $\leq$ 0.3, ***p $\leq$ 0.05).

(C) IC_{50} values (–*ln*) for taselisib plotted against CNA status of *FOXO3*. Plots and statistical analysis are as in (B).

(D) IC_{50} values (–*ln*) for pictilisib plotted against CNA status of *FOXO3*. Plots and statistical analysis are as in (B).

(E) IC_{50} values (–*ln*) for taselisib plotted against CNA status of *ECTL2L*. Plots and statistical analysis are as in (B).

(F) Trends in drug sensitivity-CNA associations predicted by direct QTL in cell line data and PDTX mice. The top-ranking CNA are reported here after filtering for those comparisons with at least four measurements in each experimental system. Plots and statistical analysis are as in (A).

predictors were not informative. We observed a correlation between fulvestrant resistance and high EGFR- and RAS-independent activation of PI3K (SERUM·PI3K), which suggests fulvestrant with a PI3K inhibitor as a potential combination therapy for fulvestrant resistance. Indeed, fulvestrant, which is used in endocrine therapy, was recently shown to be effective in postmenopausal women with endocrine-resistant, hormone-receptor-positive, and HER2-negative advanced breast cancer when used in combination with a PI3K inhibitor (Baselga et al., 2017). Furthermore, the correlation of fulvestrant resistance to p-p38 and p-SRC cellular variability suggests that a combination of fulvestrant with either a p38 or a SRC inhibitor should be effective in treatment of ER-positive breast cancer. For lapatinib, the median expression of p-SRC was predictive of resistance; therefore, it would be interesting to test the effects of a combination therapy of lapatinib with a SRC inhibitor.

Our study thus makes a case for further expanding drug sensitivity predictors with single-cell measurements, and we expect that a comprehensive signaling network model, which includes more markers covering more signaling pathways, more cell lines, and integrates signaling single-cell heterogeneity, will further increase drug sensitivity prediction accuracy. However,

measurements of patient-derived cells would be practically unfeasible, and translation of this knowledge to scalable and robust biomarkers such as genomic signatures is needed before this type of modeling will impact patient care. As a proof of concept, we identified genomic aberrations that correlated with our drug-sensitivity-predictive signaling features. We identified the known lapatinib-sensitivity-predictive *EP300* CNA (Mahmud et al., 2019) and the interesting *PPM1D* CNA, which encodes a serine threonine phosphatase amplified in approximately 8% of breast cancers (Lambros et al., 2010) and is a defining feature of IntClust1 breast cancer, an aggressive ER^+ subtype with higher risk for late relapse (Curtis et al., 2012; Rueda et al., 2019). Furthermore, the lapatinib-predictive p38·MK2 edge flux linked amplification of the breast cancer oncogene *A1CF* (Yan et al., 2017), and of *ASAH2B* to lapatinib resistance. Interestingly, the long non-coding *ASAH2B-2* was recently shown to promote breast cancer cell growth via the PI3K pathway (Li et al., 2018), supporting our findings. Furthermore, the fulvestrant-sensitivity-predictive MSK·NF-κB edge flux could be linked to the breast-cancer-proposed biomarker *MACC1* (Huang et al., 2013). The same genomic aberrations were not directly predictive of drug sensitivity, showing the importance of our characterization of cellular signaling. Our findings are consistent with the notion that multiple, potentially patient-specific mutations converge on common pathways. Thus, while individual effects of mutations may be too weak to yield statistically significant associations, multiple mutations may modify the same pathways, which enabled us to detect pathway—drug sensitivity associations.

In summary, we have used single-cell dynamic measurements of cellular signaling responses to generate mechanistic signaling network models that were predictive of breast cancer cell line resistance and sensitivity to PI3K-MTOR and other drugs. We used our models to identify genomic variants predictive of drug sensitivity. We envision that a similar approach will eventually deliver robust drug-patient matches.

STAR★METHODS

Detailed methods are provided in the online version of this paper and include the following:

- KEY RESOURCES TABLE
- RESOURCE AVAILABILITY
  - Lead contact
  - Materials availability
  - Data and code availability
- EXPERIMENTAL MODEL AND SUBJECT DETAILS
  - Cell lines
  - Patient derived tumor xenograft mouse models
- METHOD DETAILS
  - Cell line stimulation
  - Mass cytometry
  - Mass cytometry analysis
  - Mass spectrometry
  - Spectral library sample preparation
  - Peptide separation
  - Spectral library data-dependent acquisition
  - Data-independent acquisition
  - Peptide identification and spectral library
  - Breast cancer-associated proteins
  - Signaling model
  - Logic-based dynamic models
  - Cell line-specific parameter estimation
  - Mutation matrix
  - Drug sensitivity prediction
  - RNA-seq data
  - Edge flux
  - Macau
  - Identification of predictive genomic aberrations
  - Drug sensitivity determination in PDTX models
- QUANTIFICATION AND STATISTICAL ANALYSIS
  - Identification of general trends in cytometry data
  - Mass spectrometry data analysis
  - Gene ontology enrichment analysis
  - Drug sensitivity feature importance
  - Features predictive of overall sensitivity
  - Features predictive of pathway sensitivity
  - Comparison of the two QTL approaches
  - Comparison of PDTX to the cell line data

SUPPLEMENTAL INFORMATION

Supplemental information can be found online at https://doi.org/10.1016/j.cels.2021.04.002.

ACKNOWLEDGMENTS

We thank the Bodenmiller and Picotti laboratories for support and fruitful discussions, in particular, Andrea Jacobs, Stefanie Engler, and Paul Boersema for their help in running the labs. We thank Prof. Benjamin G. Neel, NYU Langone Health, and Prof. Joe Gray, Oregon Health & Science University Center for Spatial Systems Biomedicine, Portland, for providing cell lines and Jan Großbach (CECAD, University of Cologne, Germany) for support with the random forest QTL mapping. B.B. was supported by a SNSF R'Equip grant, a SNSF Assistant Professorship grant, the SystemsX Transfer Project "Friends and Foes," the SystemX grants Metastasix and PhosphoNEtX, a NIH grant (UC4 DK108132), the CRUK IMAXT Grand Challenge, and by the European Research Council (ERC) under the European Union's Seventh Framework Program (FP/2007-2013)/ERC grant agreement no. 336921. J.S.-R. was partially funded by the Joint Research Center for Computational Biomedicine (which is partially funded by Bayer AG). A. Beyer received funds from the German Federal Ministry of Education and Research (BMBF grant: PhosphoNetPPM). P.P. was supported by a Personalized Health and Related Technologies (PHRT) grant (PHRT-506) and the European Union's Horizon 2020 research and innovation program with both the European Research Council (grant agreement no. 866004) and through the EPIC-XS Consortium (grant agreement no. 823839). C.C. was supported by Cancer Research UK and by an advanced grant from the European Research Council (ERC) under the European Union's Horizon 2020 research and innovation program (ERC-2015-AdG-694620).

AUTHOR CONTRIBUTIONS

M.T., A. Beyer, P.P., J.S.-R., and B.B. conceived and designed the experiments. M.T. performed experiments. V.C. and M.T. analyzed the proteomic data. Mass cytometry data pre-processing was performed by K.C. and M.T., while A.G. built the logic models with the help of M.T.; drug sensitivity prediction was done by M.Y. with help by A.G. and M.T.; the genomic analysis was performed by J.W. and M.T. The PDTX experiments were conceived and performed by O.M.R., A. Bruna, E.E., and C.C.; M.T., N.d.S., and B.B. wrote the manuscript. All authors contributed to the manuscript.

DECLARATION OF INTERESTS

B.B. is a member of the advisory board of Cell Systems. P.P. is a scientific advisor and M.T. is an employee of Biognosys AG (Zurich, Switzerland).

J.S.-R. has received funding from GSK and Sanofi and expects consultant fees from Travere Therapeutics. C.C. is a member of Astra Zeneca's iMED External Science Panel, of Illumina's Scientific Advisory Board, and is a recipient of research grants (administered by the University of Cambridge) from AstraZeneca, Genentech, Roche, and Servier.

Received: January 21, 2020
Revised: December 16, 2020
Accepted: April 7, 2021
Published: April 30, 2021

REFERENCES

Allen, L.F., Sebolt-Leopold, J., and Meyer, M.B. (2003). CI-1040 (PD184352), a targeted signal transduction inhibitor of MEK (MAPKK). Semin. Oncol. *30* (*Suppl. 16*), 105–116.

An, X., Tiwari, A.K., Sun, Y., Ding, P.R., Ashby, C.R., and Chen, Z.S. (2010). Bcr-abl tyrosine kinase inhibitors in the treatment of Philadelphia chromosome positive chronic myeloid leukemia: a review. Leuk. Res. *34*, 1255–1268.

Barretina, J., Caponigro, G., Stransky, N., Venkatesan, K., Margolin, A.A., Kim, S., Wilson, C.J., Lehár, J., Kryukov, G.V., Sonkin, D., et al. (2012). The cancer cell line encyclopedia enables predictive modelling of anticancer drug sensitivity. Nature *483*, 603–607.

Barrette, A.M., Bouhaddou, M., and Birtwistle, M.R. (2018). Integrating transcriptomic data with mechanistic systems pharmacology models for virtual drug combination trials. ACS Chem. Neurosci. *9*, 118–129.

Baselga, J., Im, S.A., Iwata, H., Cortés, J., De Laurentiis, M., Jiang, Z., Arteaga, C.L., Jonat, W., Clemons, M., Ito, Y., et al. (2017). Buparlisib plus fulvestrant versus placebo plus fulvestrant in postmenopausal, hormone receptor-positive, HER2-negative, advanced breast cancer (BELLE-2): a randomised, double-blind, placebo-controlled, phase 3 trial. Lancet Oncol *18*, 904–916.

Beal, J., Montagud, A., Traynard, P., Barillot, E., and Calzone, L. (2019). Personalization of logical models with multi-omics data allows clinical stratification of patients. Front. Physiol. *9*, 1965.

Benjamini, Y., and Hochberg, Y. (1995). Controlling the false discovery rate: a practical and powerful approach to multiple testing. J. R. Stat. Soc. B *57*, 289–300.

Bilbao, A., Zhang, Y., Varesio, E., Luban, J., Strambio-De-Castillia, C., Lisacek, F., and Hopfgartner, G. (2015). Ranking fragment ions based on outlier detection for improved label-free quantification in data-independent acquisition LC–MS/MS. J. Proteome Res. *14*, 4581–4593.

Bodenmiller, B., Zunder, E.R., Finck, R., Chen, T.J., Savig, E.S., Bruggner, R.V., Simonds, E.F., Bendall, S.C., Sachs, K., Krutzik, P.O., and Nolan, G.P. (2012). Multiplexed mass cytometry profiling of cellular states perturbed by small-molecule regulators. Nat. Biotechnol. *30*, 858–867.

Bruderer, R., Bernhardt, O.M., Gandhi, T., Miladinović, S.M., Cheng, L.Y., Messner, S., Ehrenberger, T., Zanotelli, V., Butscheid, Y., Escher, C., et al. (2015). Extending the limits of quantitative proteome profiling with data-independent acquisition and application to acetaminophen-treated three-dimensional liver microtissues. Mol. Cell. Proteomics *14*, 1400–1410.

Bruna, A., Rueda, O.M., Greenwood, W., Batra, A.S., Callari, M., Batra, R.N., Pogrebniak, K., Sandoval, J., Cassidy, J.W., Tufegdzic-Vidakovic, A., et al. (2016). A biobank of breast cancer explants with preserved intra-tumor heterogeneity to screen anticancer compounds. Cell *167*, 260–274.e22.

Campbell, I.G., Russell, S.E., Choong, D.Y.H., Montgomery, K.G., Ciavarella, M.L., Hooi, C.S.F., Cristiano, B.E., Pearson, R.B., and Phillips, W.A. (2004). Mutation of the PIK3CA gene in ovarian and breast cancer. Cancer Res. *64*, 7678–7681.

Cancer Genome Atlas Network (2012). Comprehensive molecular portraits of human breast tumours. Nature *490*, 61–70.

Choi, J., Kim, D.H., Jung, W.H., and Koo, J.S. (2013). Differential expression of immune-related markers in breast cancer by molecular phenotypes. Breast Cancer Res. Treat. *137*, 417–429.

Chevrier, S., Crowell, H.L., Zanotelli, V.R.T., Engler, S., Robinson, M.D., and Bodenmiller, B. (2018). Compensation of Signal Spillover in Suspension and Imaging Mass Cytometry. Cell Systems *6*, 612–620.

Choi, M., Chang, C.Y., Clough, T., Broudy, D., Killeen, T., MacLean, B., and Vitek, O. (2014). MSstats: an R package for statistical analysis of quantitative mass spectrometry-based proteomic experiments. Bioinformatics *30*, 2524–2526.

Clément-Ziza, M., Marshellach, F.X., Codlin, S., Papadikas, M.A., Reinhardt, S., Rodríguez-López, M., Martin, S., Marguerat, S., Schmidt, A., Lee, E., et al. (2014). Natural genetic variation impacts expression levels of coding, non-coding, and antisense transcripts in fission yeast. Mol. Syst. Biol. *10*, 764.

Coates, A.S., Winer, E.P., Goldhirsch, A., Gelber, R.D., Gnant, M., Piccart-Gebhart, M., Thürlimann, B., and Senn, H.J.; Panel Members (2015). Tailoring therapies—improving the management of early breast cancer: St Gallen International Expert Consensus on the primary therapy of early breast cancer 2015. Ann. Oncol. *26*, 1533–1546.

Cooper, S., and Bakal, C. (2017). Accelerating live single-cell signalling studies. Trends Biotechnol. *35*, 422–433.

Costello, J.C., Heiser, L.M., Georgii, E., Gönen, M., Menden, M.P., Wang, N.J., Bansal, M., Ammad-ud-din, M., Hintsanen, P., Khan, S.A., et al. (2014). A community effort to assess and improve drug sensitivity prediction algorithms. Nat. Biotechnol. *32*, 1202–1212.

Curtis, C., Shah, S.P., Chin, S.F., Turashvili, G., Rueda, O.M., Dunning, M.J., Speed, D., Lynch, A.G., Samarajiwa, S., Yuan, Y., et al. (2012). The genomic and transcriptomic architecture of 2,000 breast tumours reveals novel subgroups. Nature *486*, 346–352.

De Andrade, J.P., Park, J.M., Gu, V.W., Woodfield, G.W., Kulak, M.V., Lorenzen, A.W., Wu, V.T., Van Dorin, S.E., Spanheimer, P.M., and Weigel, R.J. (2016). EGFR is regulated by TFAP2C in luminal breast cancer and is a target for vandetanib. Mol. Cancer Ther. *15*, 503–511.

Eduati, F., Doldàn-Martelli, V., Klinger, B., Cokelaer, T., Sieber, A., Kogera, F., Dorel, M., Garnett, M.J., Blüthgen, N., and Saez-Rodriguez, J. (2017). Drug resistance mechanisms in colorectal cancer dissected with cell type-specific dynamic logic models. Cancer Res. *77*, 3364–3375.

Erichson, N.B., Zheng, P., Manohar, K., Brunton, S.L., Kutz, J.N., and Aravkin, A.Y. (2020). Sparse principal component analysis via variable projection. SIAM J. Appl. Math. *80*, 977–1002.

Feng, L., and Chen, J. (2012). The E3 ligase RNF8 regulates KU80 removal and NHEJ repair. Nat. Struct. Mol. Biol. *19*, 201–206.

Fey, D., Halasz, M., Dreidax, D., Kennedy, S.P., Hastings, J.F., Rauch, N., Munoz, A.G., Pilkington, R., Fischer, M., Westermann, F., et al. (2015). Signaling pathway models as biomarkers: patient-specific simulations of JNK activity predict the survival of neuroblastoma patients. Sci. Signal. *8*, ra130.

Finck, R., Simonds, E.F., Jager, A., Krishnaswamy, S., Sachs, K., Fantl, W., Pe'er, D., Nolan, G.P., and Bendall, S.C. (2013). Normalization of mass cytometry data with bead standards. Cytometry A *83*, 483–494.

Folkes, A.J., Ahmadi, K., Alderton, W.K., Alix, S., Baker, S.J., Box, G., Chuckowree, I.S., Clarke, P.A., Depledge, P., Eccles, S.A., et al. (2008). The identification of 2-(1 H -indazol-4-yl)-6-(4-methanesulfonyl-piperazin-1-yl-methyl)-4-morpholin-4-yl-thieno[3,2- d]pyrimidine (GDC-0941) as a potent, selective, orally bioavailable inhibitor of class I PI3 kinase for the treatment of cancer. J. Med. Chem. *51*, 5522–5532.

Forbes, S.A., Bindal, N., Bamford, S., Cole, C., Kok, C.Y., Beare, D., Jia, M., Shepherd, R., Leung, K., Menzies, A., et al. (2011). COSMIC: mining complete cancer genomes in the catalogue of somatic mutations in cancer. Nucleic Acids Res. *39*, D945–D950.

Fröhlich, F., Kessler, T., Weindl, D., Shadrin, A., Schmiester, L., Hache, H., Muradyan, A., Schütte, M., Lim, J.-H., Heinig, M., et al. (2018). Efficient parameter estimation enables the prediction of drug response using a mechanistic pan-cancer pathway model. Cell Syst. *7*, 567–579.e6.

Garbe, C., and Eigentler, T.K. (2018). Vemurafenib. Recent Results Cancer Res. *211*, 77–89.

Garg, R., Benedetti, L.G., Abera, M.B., Wang, H., Abba, M., and Kazanietz, M.G. (2014). Protein kinase C and cancer: what we know and what we do not. Oncogene *33*, 5225–5237.

Garnett, M.J., Edelman, E.J., Heidorn, S.J., Greenman, C.D., Dastur, A., Lau, K.W., Greninger, P., Thompson, I.R., Luo, X., Soares, J., et al. (2012). Systematic identification of genomic markers of drug sensitivity in cancer cells. Nature. *483*, 570–575.

Garrett, J.T., and Arteaga, C.L. (2011). Resistance to HER2-directed antibodies and tyrosine kinase inhibitors: mechanisms and clinical implications. Cancer Biol. Ther. *11*, 793–800.

Ghandi, M., Huang, F.W., Jané-Valbuena, J., Kryukov, G.V., Lo, C.C., McDonald, E.R., Barretina, J., Gelfand, E.T., Bielski, C.M., Li, H., et al. (2019). Next-generation characterization of the cancer cell line encyclopedia. Nature *569*, 503–508.

Gholami, A.M., Hahne, H., Wu, Z., Auer, F.J., Meng, C., Wilhelm, M., and Kuster, B. (2013). Global proteome analysis of the NCI-60 cell line panel. Cell Rep. *4*, 609–620.

Giampaglia, M., Chiuri, V.E., Tinelli, A., De Laurentiis, M., Silvestris, N., and Lorusso, V. (2010). Lapatinib in breast cancer: clinical experiences and future perspectives. Cancer Treat. Rev. *36* (suppl 3), S72–S79.

Gillet, L.C., Navarro, P., Tate, S., Röst, H., Selevsek, N., Reiter, L., Bonner, R., and Aebersold, R. (2012). Targeted data extraction of the MS/MS spectra generated by data-independent acquisition: a new concept for consistent and accurate proteome analysis. Mol. Cell. Proteomics *11*, O111.016717.

Graff, J.R., McNulty, A.M., Hanna, K.R., Konicek, B.W., Lynch, R.L., Bailey, S.N., Banks, C., Capen, A., Goode, R., Lewis, J.E., et al. (2005). The protein kinase Cbeta–selective inhibitor, enzastaurin (LY317615.HCl), suppresses signaling through the AKT pathway, induces apoptosis, and suppresses growth of human colon cancer and glioblastoma xenografts. Cancer Res. *65*, 7462–7469.

Grimaldi, A.M., Simeone, E., Festino, L., Vanella, V., Strudel, M., and Ascierto, P.A. (2017). MEK inhibitors in the treatment of metastatic melanoma and solid tumors. Am. J. Clin. Dermatol. *18*, 745–754.

Gschwantler-Kaulich, D., Grunt, T.W., Muhr, D., Wagner, R., Kölbl, H., and Singer, C.F. (2016). HER specific TKIs exert their antineoplastic effects on breast cancer cell lines through the involvement of STAT5 and JNK. PLoS One *11*, e0146311.

Guo, T., Luna, A., Rajapakse, V.N., Koh, C.C., Wu, Z., Menden, M.P., Cheng, Y., Calzone, L., Martignetti, L., Ori, A., et al. (2019). Rapid proteotyping reveals cancer biology and drug response determinants in the NCI-60 cells. bioRxiv https://www.biorxiv.org/content/10.1101/268953v2.

Hass, H., Masson, K., Wohlgemuth, S., Paragas, V., Allen, J.E., Sevecka, M., Pace, E., Timmer, J., Stelling, J., Macbeath, G., et al. (2017). Predicting ligand-dependent tumors from multi-dimensional signaling features. NPJ Syst. Biol. Appl. *3*, 27.

Heiser, L.M., Sadanandam, A., Kuo, W.L., Benz, S.C., Goldstein, T.C., Ng, S., Gibb, W.J., Wang, N.J., Ziyad, S., Tong, F., et al. (2012). Subtype and pathway specific responses to anticancer compounds in breast cancer. Proc. Natl. Acad. Sci. USA *109*, 2724–2729.

Hengenius, J.B., Gribskov, M., Rundell, A.E., and Umulis, D.M. (2014). Making models match measurements: model optimization for morphogen patterning networks. Semin. Cell Dev. Biol. *35*, 109–123.

Huang, Y., Zhang, H., Cai, J., Fang, L., Wu, J., Ye, C., Zhu, X., and Li, M. (2013). Overexpression of MACC1 and its significance in human breast cancer progression. Cell Biosci. *3*, 16.

Iorio, F., Knijnenburg, T.A., Vis, D.J., Bignell, G.R., Menden, M.P., Schubert, M., Aben, N., Gonçalves, E., Barthorpe, S., Lightfoot, H., et al. (2016). A landscape of pharmacogenomic interactions in cancer. Cell *166*, 1–15.

Kim, C., and Giaccone, G. (2018). MEK inhibitors under development for treatment of non-small-cell lung cancer. Expert Opin. Investig. Drugs *27*, 17–30.

Klinger, B., Sieber, A., Fritsche-Guenther, R., Witzel, F., Berry, L., Schumacher, D., Yan, Y., Durek, P., Merchant, M., Schäfer, R., et al. (2013). Network quantification of EGFR signaling unveils potential for targeted combination therapy. Mol. Syst. Biol. *9*, 673.

Klopfenstein, D.V., Zhang, L., Pedersen, B.S., Ramírez, F., Warwick Vesztrocy, A., Naldi, A., Mungall, C.J., Yunes, J.M., Botvinnik, O., Weigel, M., et al. (2018). GOATOOLS: a Python library for gene ontology analyses. Sci. Rep. *8*, 10872.

Kotecha, N., Krutzik, P.O., and Irish, J.M. (2010). Web-based analysis and publication of flow cytometry experiments. Curr. Protoc. Cytom. *53*, 17.1–10.17.24.

Krop, I.E., Mayer, I.A., Ganju, V., Dickler, M., Johnston, S., Morales, S., Yardley, D.A., Melichar, B., Forero-Torres, A., Lee, S.C., et al. (2016). Pictilisib for oestrogen receptor-positive, aromatase inhibitor-resistant, advanced or metastatic breast cancer (FERGI): a randomised, double-blind, placebo-controlled, phase 2 trial. Lancet Oncol. *17*, 811–821.

Lambros, M.B., Natrajan, R., Geyer, F.C., Lopez-Garcia, M.A., Dedes, K.J., Savage, K., Lacroix-Triki, M., Jones, R.L., Lord, C.J., Linardopoulos, S., et al. (2010). PPM1D gene amplification and overexpression in breast cancer: a qRT-PCR and chromogenic in situ hybridization study. Mod. Pathol. *23*, 1334–1345.

Lee, M.J., Ye, A.S., Gardino, A.K., Heijink, A.M., Sorger, P.K., Macbeath, G., and Yaffe, M.B. (2012). Sequential application of anticancer drugs enhances cell death by rewiring apoptotic signaling networks. Cell *149*, 780–794.

Li, J., Kim, S.G., and Blenis, J. (2014). Rapamycin: one drug, many effects. Cell Metab. *19*, 373–379.

Li, J., Zhang, J., Jin, L., Deng, H., and Wu, J. (2018). Silencing lnc-ASAH2B-2 inhibits breast cancer cell growth via the mTOR pathway. Anticancer Res. *38*, 3427–3434.

Lun, X.K., Zanotelli, V.R.T., Wade, J.D., Schapiro, D., Tognetti, M., Dobberstein, N., and Bodenmiller, B. (2017). Influence of node abundance on signaling network state and dynamics analyzed by mass cytometry. Nat. Biotechnol. *35*, 164–172.

Lun, X.-K., Szklarczyk, D., Gábor, A., Dobberstein, N., Zanotelli, V.R.T., Saez-Rodriguez, J., von Mering, C., and Bodenmiller, B. (2019). Analysis of the human kinome and phosphatome by mass cytometry reveals overexpression-induced effects on cancer-related signaling in brief. Mol. Cell *74*, 1086–1102.e5.

Mahmud, Z., Gomes, A.R., Lee, H.J., Aimjongjun, S., Jiramongkol, Y., Yao, S., Zona, S., Alasiri, G., Gong, G., Yagüe, E., and Lam, E.W.-F. (2019). EP300 and SIRT1/6 co-regulate lapatinib sensitivity via modulating FOXO3-acetylation and activity in breast cancer. Cancers (Basel) *11*, 1067.

Marcotte, R., Sayad, A., Brown, K.R., Sanchez-Garcia, F., Reimand, J., Haider, M., Virtanen, C., Bradner, J.E., Bader, G.D., Mills, G.B., et al. (2016). Functional genomic landscape of human breast cancer drivers, vulnerabilities, and resistance. Cell *164*, 293–309.

Menden, M.P., Casale, F.P., Stephan, J., Bignell, G.R., Iorio, F., McDermott, U., Garnett, M.J., Saez-Rodriguez, J., and Stegle, O. (2018). The germline genetic component of drug sensitivity in cancer cell lines. Nat. Commun. *9*, 3385.

Meric-Bernstam, F., Akcakanat, A., Chen, H., Do, K.A., Sangai, T., Adkins, F., Gonzalez-Angulo, A.M., Rashid, A., Crosby, K., Dong, M., et al. (2012). PIK3CA/PTEN mutations and Akt activation as markers of sensitivity to allosteric mTOR inhibitors. Clin. Cancer Res. *18*, 1777–1789.

Michaelson, J.J., Alberts, R., Schughart, K., and Beyer, A. (2010). Data-driven assessment of eQTL mapping methods. BMC Genomics *11*, 502.

Michaelson, J.J., Loguercio, S., and Beyer, A. (2009). Detection and interpretation of expression quantitative trait loci (eQTL). Methods *48*, 265–276.

Mitchison, T.J. (2012). The proliferation rate paradox in antimitotic chemotherapy. Mol. Biol. Cell *23*, 1–6.

Miura, H., Kondo, Y., Matsuda, M., and Aoki, K. (2018). Cell-to-cell heterogeneity in p38-mediated cross-inhibition of JNK causes stochastic cell death. Cell Rep. *24*, 2658–2668.

Nathan, M.R., and Schmid, P. (2017). A review of fulvestrant in breast cancer. Oncol. Ther. *5*, 17–29.

Neve, R.M., Chin, K., Fridlyand, J., Yeh, J., Baehner, F.L., Fevr, T., Clark, L., Bayani, N., Coppe, J.-P., Tong, F., et al. (2006). A collection of breast cancer cell lines for the study of functionally distinct cancer subtypes. Cancer Cell *10*, 515–527.

Niepel, M., Hafner, M., Pace, E.A., Chung, M., Chai, D.H., Zhou, L., Schoeberl, B., and Sorger, P.K. (2013). Profiles of basal and stimulated receptor signaling networks predict drug response in breast cancer lines. Sci. Signal. *6*, ra84.

Nik-Zainal, S., Davies, H., Staaf, J., Ramakrishna, M., Glodzik, D., Zou, X., Martincorena, I., Alexandrov, L.B., Martin, S., Wedge, D.C., et al. (2016). Landscape of somatic mutations in 560 breast cancer whole-genome sequences. Nature *534*, 47–54.

Pennock, S., and Wang, Z. (2003). Stimulation of cell proliferation by endosomal epidermal growth factor receptor as revealed through two distinct phases of signaling. Mol. Cell. Biol. *23*, 5803–5815.

Pereira, B., Chin, S.F., Rueda, O.M., Vollan, H.K., Provenzano, E., Bardwell, H.A., Pugh, M., Jones, L., Russell, R., Sammut, S.-J., et al. (2016). The somatic mutation profiles of 2,433 breast cancers refines their genomic and transcriptomic landscapes. Nat. Commun. *7*, 11479.

Piazza, I., Kochanowski, K., Cappelletti, V., Fuhrer, T., Noor, E., Sauer, U., and Picotti, P. (2018). A map of protein-metabolite interactions reveals principles of chemical communication. Cell *172*, 358–372.e23.

Picco, G., Chen, E.D., Alonso, L.G., Behan, F.M., Gonçalves, E., Bignell, G., Matchan, A., Fu, B., Banerjee, R., Anderson, E., et al. (2019). Functional linkage of gene fusions to cancer cell fitness assessed by pharmacological and CRISPR-Cas9 screening. Nat. Commun. *10*, 2198.

Piñero, J., Bravo, À., Queralt-Rosinach, N., Gutiérrez-Sacristán, A., Deu-Pons, J., Centeno, E., García-García, J., Sanz, F., and Furlong, L.I. (2017). DisGeNET: a comprehensive platform integrating information on human disease-associated genes and variants. Nucleic Acids Res. *45*, D833–D839.

Pozniak, Y., Balint-Lahat, N., Rudolph, J.D., Lindskog, C., Katzir, R., Avivi, C., Pontén, F., Ruppin, E., Barshack, I., and Geiger, T. (2016). System-wide clinical proteomics of breast cancer reveals global remodeling of tissue homeostasis. Cell Syst. *2*, 172–184.

Reiter, L., Rinner, O., Picotti, P., Hüttenhain, R., Beck, M., Brusniak, M.Y., Hengartner, M.O., and Aebersold, R. (2011). mProphet: automated data processing and statistical validation for large-scale SRM experiments. Nat. Methods *8*, 430–435.

Remy, G., Risco, A.M., Iñesta-Vaquera, F.A., González-Terán, B., Sabio, G., Davis, R.J., and Cuenda, A. (2010). Differential activation of p38MAPK isoforms by MKK6 and MKK3. Cell. Signal. *22*, 660–667.

Roux, P.P., Shahbazian, D., Vu, H., Holz, M.K., Cohen, M.S., Taunton, J., Sonenberg, N., and Blenis, J. (2007). RAS/ERK signaling promotes site-specific ribosomal protein S6 phosphorylation via RSK and stimulates cap-dependent translation. J. Biol. Chem. *282*, 14056–14064.

Rueda, O.M., Sammut, S.J., Seoane, J.A., Chin, S.F., Caswell-Jin, J.L., Callari, M., Batra, R., Pereira, B., Bruna, A., Ali, H.R., et al. (2019). Dynamics of breast-cancer relapse reveal late-recurring ER-positive genomic subgroups. Nature *567*, 399–404.

Sanchez-Vega, F., Mina, M., Armenia, J., Chatila, W.K., Luna, A., La, K.C., Dimitriadoy, S., Liu, D.L., Kantheti, H.S., Saghafinia, S., et al. (2018). Oncogenic signaling pathways in the cancer genome atlas. Cell *173*, 321–337.e10.

Schmid, P., Pinder, S.E., Wheatley, D., Macaskill, J., Zammit, C., Hu, J., Price, R., Bundred, N., Hadad, S., Shia, A., et al. (2016). Phase II randomized preoperative window-of-opportunity study of the PI3K inhibitor pictilisib plus anastrozole compared with anastrozole alone in patients with estrogen receptor–positive breast cancer. J. Clin. Oncol. *34*, 1987–1994.

Schöffski, P., Cresta, S., Mayer, I.A., Wildiers, H., Damian, S., Gendreau, S., Rooney, I., Morrissey, K.M., Spoerke, J.M., Ng, V.W., et al. (2018). A phase Ib study of pictilisib (GDC-0941) in combination with paclitaxel, with and without bevacizumab or trastuzumab, and with letrozole in advanced breast cancer. Breast Cancer Res. *20*, 109.

Simard, F.A., Cloutier, A., Ear, T., Vardhan, H., and McDonald, P.P. (2015). MEK-independent ERK activation in human neutrophils and its impact on functional responses. J. Leukoc. Biol. *98*, 565–573.

Simm, J., Arany, A., Zakeri, P., Haber, T., Wegner, J.K., Chupakhin, V., Ceulemans, H., and Moreau, Y. (2017). Macau: scalable Bayesian factorization with high-dimensional side information using MCMC. In 2017 IEEE 27th International Workshop on Machine Learning for Signal Processing (MLSP), pp. 1–6.

Sondka, Z., Bamford, S., Cole, C.G., Ward, S.A., Dunham, I., and Forbes, S.A. (2018). The COSMIC cancer gene census: describing genetic dysfunction across all human cancers. Nat. Rev. Cancer *18*, 696–705.

Stambolic, V., and Woodgett, J.R. (1994). Mitogen inactivation of glycogen synthase kinase-3β in intact cells via serine 9 phosphorylation. Biochem. J. *303*, 701–704.

Tanos, T., Rojo, L.J., Echeverria, P., and Brisken, C. (2012). ER and PR signaling nodes during mammary gland development. Breast Cancer Res. *14*, 210.

Terfve, C., Cokelaer, T., Henriques, D., MacNamara, A., Goncalves, E., Morris, M.K., van Iersel, M., Lauffenburger, D.A., and Saez-Rodriguez, J. (2012). CellNOptR: a flexible toolkit to train protein signaling networks to data using multiple logic formalisms. BMC Syst. Biol. *6*, 133.

Türei, D., Korcsmáros, T., and Saez-Rodriguez, J. (2016). OmniPath: guidelines and gateway for literature-curated signaling pathway resources. Nat. Methods *13*, 966–967.

Tyanova, S., Albrechtsen, R., Kronqvist, P., Cox, J., Mann, M., and Geiger, T. (2016). Proteomic maps of breast cancer subtypes. Nat. Commun. *7*, 10259.

Van Der Maaten, L., and Hinton, G. (2008). Visualizing data using t-SNE. J. Mach. Learn Res. *9*, 2579–2605.

Wittmann, D.M., Krumsiek, J., Saez-Rodriguez, J., Lauffenburger, D.A., Klamt, S., and Theis, F.J. (2009). Transforming Boolean models to continuous models: methodology and application to T-cell receptor signaling. BMC Syst. Biol. *3*, 98.

Xia, W., Mullin, R.J., Keith, B.R., Liu, L.H., Ma, H., Rusnak, D.W., Owens, G., Alligood, K.J., and Spector, N.L. (2002). Anti-tumor activity of GW572016: a dual tyrosine kinase inhibitor blocks EGF activation of EGFR/erbB2 and downstream ERK1/2 and AKT pathways. Oncogene *21*, 6255–6263.

Xing, J., Ginty, D.D., and Greenberg, M.E. (1996). Coupling of the RAS-MAPK pathway to gene activation by RSK2, a growth factor-regulated CREB kinase. Science *273*, 959–963.

Yaffe, M.B. (2019). Why geneticists stole cancer research even though cancer is primarily a signaling disease. Sci. Signal. *12*, eaaw3483.

Yan, X., Li, Q., Ni, D., Xie, Y., He, Q., Wan, Q., Liu, Y., Lyu, Z., Mao, Z., and Zhou, Q. (2017). Apobec-1 complementation factor regulates cell migration and apoptosis through Dickkopf1 by acting on its 3′ untranslated region in MCF7 cells. Tumour Biol. *39*, 1010428317706218.

Yang, M., Simm, J., Lam, C.C., Zakeri, P., van Westen, G.J.P., Moreau, Y., and Saez-Rodriguez, J. (2018). Linking drug target and pathway activation for effective therapy using multi-task learning. Sci. Rep. *8*, 8322.

Yang, W., Soares, J., Greninger, P., Edelman, E.J., Lightfoot, H., Forbes, S., Bindal, N., Beare, D., Smith, J.A., Thompson, I.R., et al. (2013). Genomics of drug sensitivity in cancer (GDSC): a resource for therapeutic biomarker discovery in cancer cells. Nucleic Acids Res. *41*, D955–D961.

Yanovich, G., Agmon, H., Harel, M., Sonnenblick, A., Peretz, T., and Geiger, T. (2018). Clinical proteomics of breast cancer reveals a novel layer of breast cancer classification. Cancer Res. *78*, 6001–6010.

Zhang, S., Huang, W.C., Li, P., Guo, H., Poh, S.B., Brady, S.W., Xiong, Y., Tseng, L.M., Li, S.H., Ding, Z., et al. (2011). Combating trastuzumab resistance by targeting SRC, a common node downstream of multiple resistance pathways. Nat. Med. *17*, 461–469.

Zunder, E.R., Finck, R., Behbehani, G.K., el-Amir, A.D., Krishnaswamy, S., Gonzalez, V.D., Lorang, C.G., Bjornson, Z., Spitzer, M.H., Bodenmiller, B., et al. (2015). Palladium-based mass tag cell barcoding with a doublet-filtering scheme and single-cell deconvolution algorithm. Nat. Protoc. *10*, 316–333.

STAR★METHODS

KEY RESOURCES TABLE

REAGENT or RESOURCE	SOURCE	IDENTIFIER
Antibodies		
p-MAP2K3 (Thr222), Polyclonal	Assay Biotech	Cat# A8139; RRID: AB_10683086
Ki-67, Clone B56	BD Biosciences	Cat# 550609; RRID: AB_393778
cleaved Caspase3, Clone C92-605	BD Biosciences	Cat# 550821; RRID: AB_393906
p-AKT (Thr308), Clone D25E6	Cell Signaling Technologies	Cat# 13038S; RRID: AB_2629447
p-CREB/ATF1 (Ser133 of CREB/Ser63 of ATF1), Clone J151-21	BD Biosciences	Cat# 558436; RRID: AB_647204
p-STAT5 (Tyr694), Clone 47/Stat5	BD Biosciences	Cat# 612567; RRID: AB_399858
p-SRC (Tyr418), Clone SC1T2M3	eBioscience	Cat# 14-9034-82; RRID: AB_2572916
p-FAK (Tyr397), Polyclonal	Cell Signaling Technology	Cat# 3283; RRID: AB_2173659
p-MEK1/2 (Ser221), Clone 166F8	Cell Signaling Technology	Cat# 2338; RRID: AB_490903
p-MAPKAPK2 (Thr334), Clone 27B7	Cell Signaling Technology	Cat# 3007; RRID: AB_490936
p-p70S6K (Thr389), Clone 1A5	Cell Signaling Technology	Cat# 9206; RRID: AB_2285392
p-MKK4 (Ser257/Thr261), Clone C36C11	Cell Signaling Technology	Cat# 4514; RRID: AB_2140946
p-STAT1 (Ser727), Polyclonal	Cell Signaling Technology	Cat# 9177; RRID: AB_2197983
p-p53 (Ser15), Clone 16G8	Cell Signaling Technology	Cat# 4030; RRID: AB_10694347
p-NFkB (Ser529), Clone K10-895.12.50	BD Biosciences	Cat# 558393; RRID: AB_647284
p-p38 (Thr180/Tyr182), Clone 36/p38	BD Biosciences	Cat# 612289; RRID: AB_399606
p-AMPKa (Thr172), Clone 40H9	Cell Signaling Technology	Cat# 5256; RRID: AB_10705605
p-AKT (Ser473), Clone D9E	Cell Signaling Technology	Cat# 5012; RRID: AB_2224726
p-ERK1/2 (Thr202/Tyr204), Clone 20A	BD Biosciences	Cat# 612359; RRID: AB_399648
p-MARCKS (Ser167/170), Clone D13E4	Cell Signaling Technology	Cat# 8722; RRID: AB_10999091
cyclin B1, Clone GNS-11	BD Biosciences	Cat# 554178; RRID: AB_395289
p-GSK3b (Ser9), Clone D85E12	Cell Signaling Technology	Cat# 5558; RRID: AB_10013750
GAPDH, Clone 6C5	Thermo Fisher Scientific	Cat# AM4300; RRID: AB_2536381
p-MKK3/6 (Ser189 of MKK3/Ser207 of MKK6), Clone D8E9	Cell Signaling Technology	Cat# 12280
p-PDK1 (Ser241), Clone J66-653.44.22	BD Biosciences	Cat# 558395; RRID: AB_647291
p-BTK/ITK (Tyr551 of BTK/Tyr551 of ITK), Clone 24a/BTK	BD Biosciences	Cat# 558034; RRID: AB_2067823
p-p90RSK (Ser380), Clone D5D8	Cell Signaling Technology	Cat# 12032
p-SMAD2/3 (Ser465/467 of SMAD2/ Ser423/425 of SMAD3), Clone D27F4	Cell Signaling Technology	Cat# 8828; RRID: AB_2631089
b-catenin (Non-phospho Ser33/37/Thr41), Clone D13A1	Cell Signaling Technology	Cat# 8814; RRID: AB_11127203
p-STAT3 (Tyr705), Clone 4/P-STAT3	BD Biosciences	Cat# 612356; RRID: AB_399645
p-JNK (Thr183/Tyr185), Clone G9	Cell Signaling Technology	Cat# 9255; RRID: AB_2307321
p-HH3 (Ser28), Clone HTA28	BioLegend	Cat# 641002; RRID: AB_1227659
p-S6 (Ser235/Ser236), Clone N7-548	BD Biosciences	Custom made
cleaved PARP, Clone F21-852	BD Biosciences	Cat# 552596; RRID: AB_394437
p-RB (Ser807/811), Clone D20B12	Cell Signaling Technology	Cat# 8516; RRID: AB_11178658
p-4EBP1 (Thr37/46), Clone 236B4	Cell Signaling Technology	Cat# 2855; RRID: AB_560835
Chemicals, Peptides, and Recombinant Proteins		
Paraformaldehyde	Electron Microscopy Sciences	Cat#15710
Iridium	Fluidigm	Cat#201192A

(*Continued on next page*)

Continued

REAGENT or RESOURCE	SOURCE	IDENTIFIER
Lanthanide (III) metal isotopes as chloride salts	Fluidigm	N/A
Recombinant Murine EGF	Peprotech	Cat#315-09
Sodium deoxycholate	Sigma-Aldrich	Cat#D6750; CAS #302-95-4
TryPLE SELECT 10x	Life Technologies	Cat#50-591-353
TCEP (tris(2-carboxyethyl)phosphine hydrochloride)	Pierce	Cat#20490; CAS#51805-45-9
Iodoacetamide	Sigma-Aldrich	Cat#I1149; CAS#144-48-9
Ammonium bicarbonate	Sigma-Aldrich	Cat#09830; CAS#1066-33-7
Lysyl endopeptidase	Wako Pure Chemical Industries	Cat#125-05061
GDC-0941	LC Laboratories	Cat#G-9252
Rapamycin	LC Laboratories	Cat#R-5000
Lapatinib	LC Laboratories	Cat#L-4899
Enzastaurin	LC Laboratories	Cat#E-4506
CI-1040	Selleckchem	Cat#S1020
Formic acid 98-100%	AppliChem	Cat#A38580500
Critical Commercial Assays		
MaxPAR X8 Multimetal labeling kit	Fluidigm	Cat# 201300
BCA protein assay	Pierce	Cat#23228
CellTiter-Glo 3D Cell Viability assay	Promega	Cat#G9681
HRM calibration kit	Biognosys AG	Cat#Ki-3003
Deposited Data		
Integrated raw data and preprocessed data	This paper; and Mendeley data and Sage	https://doi.org/10.17632/gvh2vtg86r.1 and https://doi.org/10.17632/gvh2vtg86r.1
Mass spectrometry proteomics data	This paper; and ProteomeXchange Consortium	PRIDE: PXD017199
Breast carcinoma-related genes	Piñero et al., 2017	http://www.disgenet.org
Drug sensitivity data	Simm et al., 2017; Yang et al., 2013	https://www.cancerrxgene.org/
RNA-seq data	Marcotte et al., 2016	Gene Expression Omnibus (GEO): GSE73526 and GSE74702
Original code	GitHub	https://github.com/saezlab/breastCancerCytof
Code used for the generation of the figures	GitHub	https://github.com/BodenmillerGroup/Signaling-Network-Landscape-of-Breast-Cancer
Experimental Models: Cell Lines		
184A1	Benjamin G. Neel Lab (Marcotte et al., 2016)	ATCC CRL-8798
184B5	ATCC	ATCC CRL-8799
AU-565	ATCC	ATCC CRL-2351
BT-20	ATCC	ATCC HTB-19
BT-474	ATCC	ATCC HTB-20
BT-483	ATCC	ATCC HTB-121
BT-549	ATCC	ATCC HTB-122
CAL120	DSMZ	ACC 459
CAL148	DSMZ	ACC 460
CAL-51	Benjamin G. Neel Lab (Marcotte et al., 2016)	ACC-302
CAL85-1	DSMZ	ACC 440
CAMA-1	ATCC	ATCC HTB-21
DU4475	ATCC	ATCC HTB-123
EFM-19	Benjamin G. Neel Lab (Marcotte et al., 2016)	ACC 231
EFM-192A	DSMZ	ACC 258

(*Continued on next page*)

Continued

REAGENT or RESOURCE	SOURCE	IDENTIFIER
EVSA-T	DSMZ	ACC 433
HBL100	Joe W. Gray Lab (Heiser et al., 2012)	N/A
HCC1143	DSMZ	ACC 517
HCC1187	ATCC	ATCC CRL-2322
HCC1395	ATCC	ATCC CRL-2324
HCC1419	ATCC	ATCC CRL-2326
HCC1428	ATCC	ATCC CRL-2327
HCC1500	ATCC	ATCC CRL-2329
HCC1569	ATCC	ATCC CRL-2330
HCC1599	ATCC	ATCC CRL-2331
HCC1806	ATCC	ATCC CRL-2335
HCC1937	ATCC	ATCC CRL-2336
HCC1954	ATCC	ATCC CRL-2338
HCC202	ATCC	ATCC CRL-2316
HCC2157	ATCC	ATCC CRL-2340
HCC2185	Joe W. Gray Lab (Heiser et al., 2012)	N/A
HCC2218	ATCC	ATCC CRL-2343
HCC3153	Gray	
HCC38	ATCC	ATCC CRL-2314
HCC70	ATCC	ATCC CRL-2315
HDQ-P1	DSMZ	ACC 494
Hs 578T	ATCC	ATCC HTB-126
JIMT-1	DSMZ	ACC 589
KPL-1	Benjamin G. Neel Lab (Marcotte et al., 2016)	ACC 317
LY2	Joe W. Gray Lab (Heiser et al., 2012)	N/A
MA-CLS-2	CLS	300271
MCF10A	ATCC	ATCC CRL-10317
MCF10F	ATCC	ATCC CRL-10318
MCF12A	ATCC	ATCC CRL-10782
MCF7	ATCC	ATCC HTB-22
MDA-kb2	ATCC	ATCC CRL-2713
MDA-MB-134-VI	ATCC	ATCC HTB-23
MDA-MB-157	ATCC	ATCC HTB-24
MDA-MB-175-VII	ATCC	ATCC HTB-25
MDA-MB-231	ATCC	ATCC HTB-26
MDA-MB-361	ATCC	ATCC HTB-27
MDA-MB-415	ATCC	ATCC HTB-128
MDA-MB-436	ATCC	ATCC HTB-130
MDA-MB-453	ATCC	ATCC HTB-131
MDA-MB-468	ATCC	ATCC HTB-132
MFM-223	DSMZ	ACC 422
MPE600	Joe W. Gray Lab (Heiser et al., 2012)	N/A
MX1	CLS	300296
OCUB-M	RIKEN	RCB0881
SK-BR-3	ATCC	ATCC HTB-30
T47D	ATCC	ATCC HTB-133
UACC3199	ATCC	ATCC CRL-2983
UACC-812	ATCC	ATCC CRL-1897
UACC-893	ATCC	ATCC CRL-1902
ZR-75-1	ATCC	ATCC CRL-1500

(*Continued on next page*)

Continued

REAGENT or RESOURCE	SOURCE	IDENTIFIER
ZR-75-30	ATCC	ATCC CRL-1504
ZR-75-B	Joe W. Gray Lab (Heiser et al., 2012)	N/A
184A1	Benjamin G. Neel Lab (Marcotte et al., 2016)	ATCC CRL-8798
184B5	ATCC	ATCC CRL-8799
AU-565	ATCC	ATCC CRL-2351
BT-20	ATCC	ATCC HTB-19
BT-474	ATCC	ATCC HTB-20
Experimental Models: Organisms/Strains		
NSG mice	obtained from Charles Rivers (Bruna et al., 2016)	NOD.Cg-Prkdcscid Il2rgtm1Wjl/SzJ
AB040, Metastatic	Carlos Caldas Lab (Bruna et al., 2016)	N/A
AB521M, Metastatic	Carlos Caldas Lab (Bruna et al., 2016)	N/A
AB551, Metastatic	Carlos Caldas Lab (Bruna et al., 2016)	N/A
VHIO244, Metastatic	Carlos Caldas Lab (Bruna et al., 2016)	N/A
VHIO179, Metastatic	Carlos Caldas Lab (Bruna et al., 2016)	N/A
VHIO124, Metastatic	Carlos Caldas Lab (Bruna et al., 2016)	N/A
VHIO098, Primary	Carlos Caldas Lab (Bruna et al., 2016)	N/A
VHIO093, Primary	Carlos Caldas Lab (Bruna et al., 2016)	N/A
STG335, Primary	Carlos Caldas Lab (Bruna et al., 2016)	N/A
STG331, Primary	Carlos Caldas Lab (Bruna et al., 2016)	N/A
STG321, Primary	Carlos Caldas Lab (Bruna et al., 2016)	N/A
STG316, Primary	Carlos Caldas Lab (Bruna et al., 2016)	N/A
STG282, Metastatic	Carlos Caldas Lab (Bruna et al., 2016)	N/A
STG282, Metastatic	Carlos Caldas Lab (Bruna et al., 2016)	N/A
STG201, Metastatic	Carlos Caldas Lab (Bruna et al., 2016)	N/A
STG195, Metastatic	Carlos Caldas Lab (Bruna et al., 2016)	N/A
STG143, Primary	Carlos Caldas Lab (Bruna et al., 2016)	N/A
STG139, Primary	Carlos Caldas Lab (Bruna et al., 2016)	N/A
IC007, Primary	Carlos Caldas Lab (Bruna et al., 2016)	N/A
HCI010, Metastatic	Carlos Caldas Lab (Bruna et al., 2016)	N/A
HCI009, Metastatic	Carlos Caldas Lab (Bruna et al., 2016)	N/A
HCI005, Metastatic	Carlos Caldas Lab (Bruna et al., 2016)	N/A
HCI001, Primary	Carlos Caldas Lab (Bruna et al., 2016)	N/A
CAMBMT1, Metastatic	Carlos Caldas Lab (Bruna et al., 2016)	N/A
AB636, Metastatic	Carlos Caldas Lab (Bruna et al., 2016)	N/A
AB630, Metastatic	Carlos Caldas Lab (Bruna et al., 2016)	N/A
AB582, Primary	Carlos Caldas Lab (Bruna et al., 2016)	N/A
AB559, Primary	Carlos Caldas Lab (Bruna et al., 2016)	N/A
AB555B, Metastatic	Carlos Caldas Lab (Bruna et al., 2016)	N/A
Software and Algorithms		
Cytobank	Cytobank	https://www.cytobank.org/
Concatenation tool	Cytobank	https://support.cytobank.org/hc/en-us/articles/206336147-FCS-file-concatenation-tool
Normalizer	Finck et al., 2013	https://github.com/nolanlab/bead-normalization/releases
Single cell debarcoder	Zunder et al., 2015	https://github.com/nolanlab/single-cell-debarcoder
t-SNE	Van Der Maaten and Hinton, 2008	https://github.com/jkrijthe/Rtsne
OmniPath	Türei et al., 2016	http://omnipathdb.org/

(*Continued on next page*)

Continued

REAGENT or RESOURCE	SOURCE	IDENTIFIER
Spectronaut v. 11.0	Biognosys AG	https://biognosys.com/
Proteome discoverer v. 2.2	ThermoFisher Scientific	https://www.thermofisher.com/us/en/home.html
RFQTL R package	Michaelson et al., 2010	http://cellnet-sb.cecad.uni-koeln.de/resources/qtl-mapping/
flowCore R package	Bioconductor	http://www.bioconductor.org/packages/release/bioc/html/flowCore.html
MSstats R package	Bioconductor	https://www.bioconductor.org/packages/release/bioc/html/MSstats.html

RESOURCE AVAILABILITY

Lead contact

Further information and requests for resources and reagents should be directed to and will be fulfilled by the Lead Contact, Bernd Bodenmiller (bernd.bodenmiller@uzh.ch).

Materials availability

This study did not generate new unique reagents.

Data and code availability

The mass spectrometry proteomics source data have been deposited at ProteomeXchange Consortium via the PRIDE partner repository and are publicly available under the accession number PRIDE: PXD017199. The mass cytometry data and other analyses including all cell-line-specific logic-based models and drug sensitivity predictions source data have been deposited at Sage and Mendeley Data and are publicly available at SAGE: https://www.synapse.org/#Synapse:syn20825065 and Mendeley Data: https://doi.org/10.17632/gvh2vtg86r.1, respectively. Furthermore, this paper analyzes existing, publicly available data. These datasets' accession numbers are provided in the key resource table.

Logic-based dynamic models and drug sensitivity prediction original code is publicly available at GitHub (https://github.com/saezlab/breastCancerCytof).

The scripts used to generate the figures reported in this paper are available at GitHub (https://github.com/BodenmillerGroup/Signaling-Network-Landscape-of-Breast-Cancer).

Any additional information required to reproduce this work is available from the Lead Contact.

EXPERIMENTAL MODEL AND SUBJECT DETAILS

Cell lines

Cells were obtained from suppliers or collaborators listed in Table S4. With the exception of BT-474 cells, all were grown according to the supplier's recommendation, and the maximum passage number was kept low (<15). Culture conditions are provided in Table S5. All cells were free of mycoplasma. For passaging, cells were incubated with 0.25% trypsin (Gibco) at 37 °C for 1 to 9 minutes depending on the cell line.

Patient derived tumor xenograft mouse models

The generation of viable cells from PDTX model tumors was done as previously described (Bruna et al., 2016). Briefly, surgically resected primary breast cancer tissue, metastasis biopsies, and pleural effusions samples were obtained from consenting patients with the appropriate approval by the National Research Ethics Service, Cambridgeshire 2 REC (REC reference number: 08/H0308/178). While tissue samples were embedded in matrigel and implanted subcutaneously into 2-4 female severe immune compromised NSG mice, pleural effusion samples were centrifuged, washed twice with water, before resuspension in 50% matrigel:FBS solution and subcutaneous injection into mice. PDTXs were implanted into multiple hosts to allow in vivo expansion and xenograft samples were cryopreserved in liquid nitrogen and freezing media (FBS/10%DMSO). All animal experiments were conducted in compliance with the rigorous Home Office framework of regulations (Project License P1266F82E). All members of the Caldas team in Cambridge adhere to Home Office Regulations and the CI has a governing committee overseeing all activities in this area.

METHOD DETAILS

Cell line stimulation

Cells were plated either in 150-mm or 100-mm dishes to achieve about 60% confluency at the time of analysis (maximum number of passages: 15). Cells were grown for 48 to 72 hours and then washed twice with PBS before starving them in serum-free medium without additives overnight before fixation for the time point zero profiling, stimulation, or treatment with inhibitor. For stimulation, EGF (Peprotech) and fetal bovine serum (FBS, Gibco) were added to final concentrations of 100 ng/ml and 10% v/v, respectively. For analysis of cells in the unstimulated state, starvation medium was replaced by complete medium. For experiments with inhibitor, the inhibitor was added 15 minutes before the addition of EGF and FBS. Inhibitors were diluted into starvation medium at approximately 100 fold the reported IC_{50} (Table S3). At 1 hour before a time point, 5-iodo-2'-deoxyuridine was added to the medium at the final concentration of 4 μM. At 5 minutes before a time point, the dish was washed and then incubated with 2X TrypLE™ Express (Life Technologies) to induce cell detachment. At the time point, dishes were scraped and paraformaldehyde (PFA, from Electron Microscopy Sciences) was added to the cell suspension to 1.6% v/v, and cells were incubated at room temperature for 10 minutes. If EGF stimulation was not necessary, cells were harvested and crosslinked with PFA either immediately after or 15 minutes after inhibitor addition. PFA was then quenched with 40% w/v bovine serum albumin (BSA, Sigma) and after centrifugation, methanol chilled to -20 °C was used to resuspend the cells for long-term storage at -80 °C. Two individual experimental replicates (referred to as A and B) with partly overlapping time points (Table S2) were performed for each cell line. For each replicate, the experimental procedures were performed on different days.

For the proteomic samples, cells were grown and collected in parallel with the replicates A and B. The third biological replicate (referred to as C) was grown independently and was passaged two more times to test for proteome stability over a limited number of cell divisions. Cells were plated in 150-mm dishes, grown for 48 to 72 hours, washed twice with PBS before addition of fresh complete growth medium overnight, washed, incubated with TrypLE™, and scraped. The sample was then washed with cold starvation medium, re-suspended in cold PBS, and sodium deoxycholate (DOC, from Sigma-Aldrich) was added to a final 5% w/w. The lysis was completed by on-ice sonication (2x30 seconds) and snap freezing in liquid nitrogen, before long-term storage at -80 °C.

Mass cytometry

Antibody conjugation

The isotope-labeled antibodies (Table S1) were generated using the MaxPAR antibody conjugation kit (Fluidigm) using the manufacturer's standard protocol. After conjugation, antibody concentrations were determined based on absorbance at 280 nm. Candor PBS Antibody Stabilization solution was used to dilute antibodies prior to long-term storage at 4 °C. Antibody target specificity was previously confirmed (Lun et al., 2017) and optimal concentrations were determined by titration.

Barcoding and staining protocol

The crosslinked and methanol-permeabilized cells were washed once with CSM (PBS with 0.5% w/v BSA, 2 mM EDTA) and once with PBS. Cells were incubated in PBS containing a barcoding reagent designed for a 126-well barcoding, containing four out of the nine metals used. Palladium (^{105}Pd, ^{106}Pd, ^{108}Pd, ^{110}Pd, Fluidigm) was used in conjunction with the chelating agent bromoacetamidobenzyl-EDTA (Dojindo); indium (^{113}In, ^{115}In, Fluidigm), yttrium, rhodium, and bismuth (^{89}Y, ^{103}Rh, ^{209}Bi, Sigma Aldrich) were chelated to maleimido-mono-amide-DOTA (Macrocyclics). The samples were randomly distributed across the wells and incubated for 30 minutes at room temperature at 100 nM metal concentrations except for bismuth (20 nM), indium isotope 113 (200 nM), and rhodium (2 μM). After incubation, the sample was washed four times with CSM (Bodenmiller et al., 2012), pooled, and stained with the metal-conjugated antibody mix at 4 °C for 1 hour. The antibody mix was removed by washing cells three times with CSM. For DNA staining, iridium-containing nucleic acid intercalator (^{191}Ir and ^{193}Ir, Fluidigm) diluted in PBS with 1.6% PFA was added to the cells to a final concentration of 500 μM, and cells were incubated at 4 °C overnight. The following day, the intercalator solution was removed, cells washed sequentially with CSM, PBS, and ddH_2O and stained for cell volume with 12.5 μg/ml bis(2,2'-bipyridine)-4'-methyl-4-carboxybipyridine-ruthenium-N-succidimyl ester-bis(hexafluorophosphate) (^{96}Ru, $^{98\text{-}102}$Ru, ^{104}Ru, Sigma Aldrich) in 0.1 M sodium hydrogen carbonate, pH 8.3 (Sigma Aldrich) for 10 minutes at room temperature. Subsequently, samples were washed once each with CSM, PBS, and ddH_2O. After the last washing step, cells were resuspended in cell running buffer (Fluidigm) and EQ™ Four Element Calibration Beads (Fluidigm) were added in a 1:10 ratio (v/v). Subsequently, samples were filtered through a 35-μm strainer just before the mass-cytometry measurement.

Mass cytometry analysis

Samples were analyzed on an upgraded CyTOF2 (Fluidigm) using the Super Sampler (Victorian Airship) introduction system. The manufacturer's standard operation procedures were used for acquisition at a cell rate of ~300 cells per second. After the acquisition, all FCS files from the same barcoded sample were concatenated as previously described (Bodenmiller et al., 2012), data were then normalized, and bead events were removed (Finck et al., 2013). A doublet-filtering scheme and single-cell deconvolution algorithm (Zunder et al., 2015) were used to achieve doublet removal and for de-barcoding of cells into their corresponding wells. Subsequently, data were processed using Cytobank (Kotecha et al., 2010). Additional gating on the DNA channels (^{191}Ir and ^{193}Ir) was used to remove remained doublets, debris, and contaminating particulates. FCS files were exported and loaded into R for downstream analysis (*flowCore* Bioconductor/R-package).

Firstly, compensation for channel crosstalk was performed using single-stained polystyrene beads (Chevrier et al., 2018). Secondly, samples that were measured multiple times were combined and the coefficients of variation (cellular variability) were computed. Thirdly, signal intensities per channel were arcsinh-transformed (asinh(x+1), *flowCore* Bioconductor/R-package) and the median computed. Fourthly, to control for batch effects, all cell lines were processed, stained, and measured together with five samples that served as technical replicates. The technical replicates were generated in large batches from two cell lines (HCC70 and MDA-MD-453) prepared at different time points to ensure negative and positive controls for each measured marker. The simultaneous processing enabled direct quantitative comparisons within a cell line and the technical replicates enabled identification of batch effects and were used in batch-correction quality control. Both the t-SNE algorithm (Van Der Maaten and Hinton, 2008) (*Rtsne* R-package) and principal component analysis (PCA, *sparsepca* R-package) were used for identification of batch effects. While the cellular variability showed no detectable batch effect, the median showed an overall loss in signal strength between the first fifteen measured cell lines and the rest (likely due to antibody aging). Centering the two batches to the common average (μ_{total}) for each median value ($x_{centered} = x - \mu_{batch} + \mu_{total}$) prevented the formation of batch-specific clusters by both PCA and t-SNE. Fifthly, the biological replicates (time course A and B, which had only partially overlapping time points) were integrated into one consensus measurement. The two time courses were centered by subtracting the means of the individual time courses and addition of the overall mean. Finally, the unmeasured time points were linearly interpolated using the R function *approxfun* (the same process was used for missing or slightly different time points) and the averages between the two biological replicates were computed. For the time point 60 minutes, sampled only in time course B, the value for the time course B was taken directly without extrapolating a value for the second time course.

Mass spectrometry

Digestion

Cell lysates from independent biological replicates were aliquoted in equivalent volumes containing 100 μg of proteome sample (quantified with a BCA assay). The samples were then reduced with 5 mM Tris(2-carboxyethyl)phosphine (ThermoFisher Scientific) for 30 minutes at 37 °C and then alkylated in the dark for 30 minutes at 25 °C with 40 mM iodoacetamide (Sigma Aldrich). Samples were diluted with 0.1 M ammonium bicarbonate (Sigma Aldrich) to a final concentration of 1% DOC before overnight digestion at 37 °C with lysyl endopeptidase (Wako Chemicals) and sequencing-grade porcine trypsin (Promega) at an enzyme-substrate ratio of 1:100 for both. Trypsin was inactivated by adding formic acid (AppliChem) to a final concentration of 1% v/v, and the precipitated DOC was removed by centrifugation. The acidified peptide mixtures were loaded into 96-well elution plates (Waters), desalted, and eluted with 80% acetonitrile. Samples were dried in a vacuum centrifuge, solubilized in 0.1% formic acid, and analyzed by mass spectrometry.

Spectral library sample preparation

The spectral libraries were obtained from all cell lines with at least three biological replicates (12 cell lines) or with eight fractions from two independent cell line pools. The cell lines pools were composed of 27 and 28 cell lines, respectively. The four central fractions were measured twice. The fractionation was performed using the Pierce™ high pH, reversed-phase peptide fractionation kit (Thermo Fisher Scientific), and iRT peptides (Biognosis AG) were added.

Peptide separation

Digested samples were analyzed on an Orbitrap Q Exactive Plus mass spectrometer (Thermo Fisher Scientific) equipped with a nano-electrospray ion source and a nano-flow LC system (Easy-nLC 1000, Thermo Fisher Scientific). Peptide separation was performed on a 40 cm x 0.75 μm i.d. column (New Objective, PF360-75-10-N-5) in-house packed with 1.9-μm C18 beads (Dr. Maisch Reprosil-Pur 120) and heated to 50 °C. Buffer A was 0.1% w/v formic acid, and buffer B was 0.1% w/v formic acid in acetonitrile. The flow rate was 300 nL/min. The gradient was as follows (buffer B in buffer A): linear from 5% to 25% over 100 minutes, 25% to 40% over 10 minutes, and 40% to 90% over 5 minutes, finishing with isocratic 90% for 5 minutes.

Spectral library data-dependent acquisition

For the spectral library, the 55 samples were analyzed by shotgun LC-MS/MS data dependent acquisition (DDA) by injection of 1 μL peptide digests at a concentration of 1 μg/μL. The MS1 spectra were acquired from 350 to 1,500 m/z at a resolution of 70,000, and the 20 most intense precursors exceeding 1,300 ion counts were selected for fragmentation at 25 eV normalized collision energy. The MS2 spectra were acquired at a resolution of 17,500 with maximally 100,000 ions, collected for 55 ms maximally. All multiply charged ions triggered MS-MS scans followed by a 30-second dynamic exclusion, and singly charged precursor ions and ions of undefinable charged states were excluded from fragmentation.

Data-independent acquisition

After addition of iRT peptides (Biognosys AG), 1 μL of peptide digest from each biological replicate was injected independently at a concentration of 1 μg/μL and measured in data-independent acquisition (DIA) mode. The DIA-MS method was as previously described (Piazza et al., 2018). Briefly, an MS1 survey scan was performed from 350 to 1,500 m/z at a resolution of 70,000 with AGC target of 3×10^6 and a 120-ms injection time. The twenty variable-width windows optimized to equally distribute the number of precursor ions had a 1 m/z overlap. MS2 spectra were acquired at a resolution of 35,000 with a fixed first mass of 150 m/z and

an AGC target of 1×10^6. In order to mimic DDA fragmentation, the normalized collision energy was 25 eV based on the doubly charged center m/z of the isolation window. The maximum injection times were automatically chosen to maximize parallelization resulting in an approximate 3-second duty cycle.

Peptide identification and spectral library

The DDA spectra were searched against the canonical Human Uniprot fasta database (version August 2018) using the Sequest HT database search engine in Protein Discoverer (version 2.2.0.388, Thermo Fisher Scientific). We allowed for up to two missed cleavages, excluded cleavage of KP and RP peptide bonds and applied a full tryptic digestion rule. Cysteine carboxyamidomethylation (+57.021 Da) and methionine oxidation (+15.995) were allowed as static and dynamic modifications, respectively. Monoisotopic peptide tolerance was set to 10 ppm, and fragment mass tolerance to 0.02 Da. The identified proteins were filtered using the high peptide confidence setting (1% false discovery rate (FDR) on peptide level). For generation of the spectral library the DDA spectra analyzed as described above were imported in the software Spectronaut Pulsar (11.0.18108.11.30271 Asimov, Biognosys AG) (Bruderer et al., 2015).

Breast cancer-associated proteins

The list of curated breast carcinoma-related genes was downloaded from the human disease discovery platform Disgenet (http://www.disgenet.org/, *curated_gene_disease_associations.tsv* file, downloaded on April 12, 2018) (Piñero et al., 2017). We included in the list genes annotated to the following breast-cancer disease categories: 'Malignant neoplasm of breast', 'Breast Cancer, Familial', 'Hereditary Breast and Ovarian Cancer Syndrome', 'Breast Carcinoma', 'Breast Neoplasms, Male', 'Invasive Ductal Breast Carcinoma', 'Inflammatory Breast Carcinoma', and 'Breast Diseases'. The list includes a total of 53 genes among which 38 are associated with significant changes in protein abundance in one or multiple cell lines.

Signaling model

We utilized the logic-based ordinary differential equation (ODE) formalism (Terfve et al., 2012) to model the signaling network of each cell line. This is a semi-mechanistic approach that combines perturbation data with prior knowledge, such as protein-protein interactions. The goal was to describe the signal transduction upon perturbation through protein activation cascades.

Logic-based dynamic models

First, we built a prior knowledge network (PKN) that contains nodes (protein markers); signed, directed edges (interactions of the proteins from Omnipath); and logical gates (AND, OR) reported in a simple interaction file (SIF) that contains three columns: source node, interaction type (activation or inhibition), and target node (Türei et al., 2016) (Figure S3A and Table S6). This PKN was built around the measured and perturbed proteins in the experiments and was used for all cell lines. Next, the PKN was translated into a dynamic ODE model using the CNORode modeling package (https://github.com/saezlab/CNORode) that is part of the CellNOpt family (Terfve et al., 2012). The node *I* property $x_i \in [0,1]$, $i = 1 \ldots N$ in the network, the differential equation was written as in Equation 1.

$$\frac{dx_i}{dt} = \tau_i\left(B_i\left(f_{1,i}(x), \ldots f_{j,i}(x), \ldots f_{N,i}(x)\right) - x_i\right) \quad \text{(Equation 1)}$$

τ_i is the responsiveness parameter of the node x_i, and a larger value results in a faster response to change in the node. B_i is the continuous Boolean function: $B_i : [0,1]^N \rightarrow [0,1]$. This function accounts for the AND and OR gates of the incoming edges on node *i* (Wittmann et al., 2009). $f_{ij}(x)$ is the transfer function from node *j* to node *i*; it describes how node *I* depends on node *j*, here we use a version of the previously described Hill-type function (Eduati et al., 2017) as shown in Equation 2.

$$f_{ij}(x) = 1 - \frac{(1-x)^{n_{ij}}}{(1-x)^{n_{ij}} + k_{ij}^{n_{ij}}}\left(1 + k_{ij}^{n_{ij}}\right) \quad \text{(Equation 2)}$$

This function has a sigmoidal-shape characterized by the free parameters κ_{ij} and n_{ij}. The trajectories are constrained in the [0-1] interval. The extreme case of 0 means that the corresponding node is inactive or inhibited, and 1 means that the node is fully activated. In order to compare the experimental measurements with the simulation results, the data were scaled to the [0-1] interval. Each marker was scaled separately across all cell lines and conditions, but different markers were not compared due to differences in sensitivity. First, the median data were scaled to the 0-1 range using the 99% interquartiles, as described in Equation 3.

$$\tilde{x} = \frac{x - x_{.005}}{x_{.995} - x_{.005}} \quad \text{(Equation 3)}$$

Values >1 or <0 were set to 1 and 0, respectively. For each experimental condition, the corresponding states in the model were adjusted. For instance, application of the stimulation was modeled by setting the input nodes to 1, and inhibition was modeled by setting the inhibited nodes to 0.

Cell line-specific parameter estimation

All the cell-line models were built from the same PKN, and 67 cell line-specific ODE models were generated. In these models there were four types of unknown parameters: initial conditions for unmeasured states (11 parameters), node responsiveness parameters

(τ_i) for each node (40 parameters), edge parameters n (88 parameters), and edge parameters κ (88 parameters). In order to reduce complexity, we fixed the values of the n parameters to 3, since they influence the outputs the least. Then we trained the ODE models using the CNORode package, following the standard approach with minor improvements. In short, the package relies on the MEIGOR optimization toolbox to find the parameter values that results in the best fit (measured by the root mean squared error, RMSE) (Terfve et al., 2012). We applied L2 regularization in the optimization as previously introduced to the CNORode (Eduati et al., 2017) to cope with non- identifiability of estimated parameters and to reduce overfitting. We evaluated five cell-line models for tuning the regularization parameter. The value of $1x10^{-5}$ for the regularization parameter resulted in a good balance between sparsity and fit (data not shown). Each model was trained using the global optimiser enhanced Scatter Search (eSS) together with the Dynamic Hill Climbing local search algorithm with 10 optimizations, 20 minutes each (as implemented in the MEIGOR package). After the optimization, the model simulation was plotted against the data to evaluate the fitting quality. To control for the model quality both the r^2 as well as the root mean square error (RMSE) were evaluated. The biological variance was computed as the RMSE between the median and the single biological replicates. The random model was made the same way as the cell line models for all cell lines, but parameters were randomly generated and not optimized.

Mutation matrix

To determine the mutational status, the SNP-specific genotype as defined by the Illumina HumanOmni1-Quad v1.0 Multi-UseManifest File (http://emea.support.illumina.com/downloads/humanomni1-quadv1_mu_product_files.html, downloaded on July 18, 2019) was mapped to the NCBI 37.1 (GRCh37) genome build taking into account ambiguous IUPAC notations and indel information. Subsequently, a cell line × SNP mutation matrix was constructed, where elements denote the fraction of alleles for which the cell line genotype mismatches the reference genotype for the respective SNP. Finally, two gene-level mutation matrices were obtained by first mapping the SNP entries to genes using the *pyensembl* package (Ensembl release 55) and then counting the values exceeding the threshold q (q = 0.5 for a ''dominant'' matrix and q = 1 for a ''recessive'' one) for each cell line and gene.

Drug sensitivity prediction

We predicted the response (-ln IC_{50}) using Macau for each drug (409 vectors of -ln IC_{50} values for 347 individual compounds) in 48 cell lines (training) with data available in the GDSC dataset (Simm et al., 2017; Yang et al., 2013). A 5-fold cross-validation and 40 iterations were used to obtain an average prediction performance (performance score) and an adjusted p-value for each predictor (Benjamini and Hochberg, 1995). As input for the drug response prediction we selected the RNA-seq filtered for exons (Marcotte et al., 2016), the protein abundance ratio, the estimated parameters (model parameters), the single-cell coefficient of variation (cellular variability), the median marker expression (median), and the edge flux.

RNA-seq data

The RNA-seq data are from a published dataset that used the same cell lines (Marcotte et al., 2016). For these cell lines, RNA-seq results tend to be consistent as long as the cells are at low passage (Peter Sorger, personal communication). The cell lines in our study were either from the same batch as the RNA-seq study (Table S4) or were purchased at a comparable passage number as that in our study. The passage number averaged 8 in our study and was 10 or lower in the RNA-seq study (Richard Marcotte and Benjamin Neel, personal communication). Furthermore, the correlation between RNA-seq and proteomics data was in the expected range (data not shown).

Edge flux

The edge fluxes were computed as the time-dependent edge strengths, or in other words the transfer function from node j to node l determined as describe by Equation 2, for each specific condition (treatment and time). This equation describes how much a node is influenced by its upstream nodes at a certain time and treatment condition. The edge flux value depends on the model parameters as well as on the activity of the influencing/upstream nodes (x, Equation 3) and can be seen as the signaling flux of the edges at a specific time and treatment condition. For the *AND*-gated edges, the edge flux is the product of two f-functions (Equation 2). For instance, $AKT,RAS \cdot MEK^{S221}$ integrates positive RAS as well as negative AKT influence and is therefore influenced by both $f_{AKT}(x_{AKT})$ and $f_{RAS}(x_{RAS})$ as follows: $AKT,RAS \cdot MEK^{S221} = (1\text{-}f_{AKT}) * f_{RAS}$.

Macau

Macau is a machine-learning approach based on scalable Bayesian multi-relational factorization with side information using Markov chain Monte Carlo Macau (MCMC) sampling that incorporates information in rows and/or columns to improve the accuracy of the predictions (Simm et al., 2017). Cell line-specific information was transformed into a matrix of L latent dimension (set to 10 as we only used cell line features) by a link matrix. Drug response was then computed by a matrix multiplication of the two latent matrices, from drug (L_{drug}) and cell lines (L_{cell}) sides. Macau employs Gibbs sampling to sample both the latent vectors and the link matrix, which connects the additional information to the latent vectors. For MCMC sampling, we chose a burn in of 400 samples, then collected 600 samples. After collection of each sample, we predicted drug response by multiplying the two latent matrices and then averaged across all 600 samples. We used a 5-fold cross-validation and iterated 40 times for an average prediction performance

(performance score) (Simm et al., 2017; Yang et al., 2018). For prediction of responses of cells lines not part of the training exercise, we used the same strategy except that inside the cross validation loop we predicted not on the test set but on the 19 hold-out cell lines.

Identification of predictive genomic aberrations

Mapping of quantitative trait loci (QTLs) was conducted using random forest ensemble learning (Michaelson et al., 2009), an approach that has been shown to outperform legacy and other multi-locus QTL mapping methods (Michaelson et al., 2010). Briefly, a random forest classifier was trained on genetic markers to predict relevant signaling features, and resulting marker selection frequencies were used as a measure for the strength of the respective QTL. Separate analyses were conducted for genotype matrices assembled from publicly available SNP (for 61 cell lines) and CNA (for 64 cell lines) data obtained using Illumina HumanOmni1-Quad BeadChips (Marcotte et al., 2016). Gene-level CNA data was discretized by thresholding CBS-segmented log-R ratios at −0.2 and 0.2. Genetic markers were filtered for mutations in cancer-driver genes (Forbes et al., 2011; Sondka et al., 2018). Markers with missing values for more than half of the cell lines and markers with a major allele frequency larger than 0.9 were excluded, resulting in 736 SNPs and 518 CNAs. The proportion of genotypic variance included in the estimated population-structure covariates was set to 0.75. Mapping scores were computed by training 10 random forests (representing independent imputations of missing marker values), each comprising 1,000 trees. To determine the significance of identified QTLs, an empirical null distribution of marker selection frequencies was estimated by repeating this step 5,000 times for 100 independent phenotype vector shuffles, totaling 5 billion randomized trees per analyzed experimental condition. The product of zero-clipped permutation importance (PI) and average increase in node purity (RSS), normalized across traits, was used as a readout for feature importance. Finally, empirical p-values adjusted for multiple testing were computed and checked for convergence by plotting them against the number of batches at varying intervals (Benjamini and Hochberg, 1995). All computations were conducted using modified versions of the *RFQTL* and *RandomForest* R packages and executed in parallelized fashion on local cloud infrastructure (Michaelson et al., 2010). Due to the small dataset used we selected a permissive adjusted p-value cutoff of 0.3. The same method, cutoffs, and selection of genomic aberrations were used for a QTL analysis on the IC_{50} values (*–ln*) for pictilisib, fulvestrant, and lapatinib in 42 and 40 cell lines for the CNAs and SNPs, respectively.

Drug sensitivity determination in PDTX models

The PDTX model tumors drug screening was done as previously described (Bruna et al., 2016). Briefly, single-cell suspensions generated from PDTX tissues were cultured into 384-well plates (25,000 cells/well). Drugs were added 24 hours after seeding and cell viability reading intensities were obtained six days post-treatment using the CellTiter-Glo 3D Cell Viability assay (Promega). The dose-response fitting was performed using isotonic regression and the IC_{50} values were predicted by fitting a smoothing spline to the isotonic regression line.

QUANTIFICATION AND STATISTICAL ANALYSIS

Identification of general trends in cytometry data

To characterize the general signaling response across all 67 cell lines we performed a two-way ANOVA comparing treatment and time (with an interaction term). The obtained p-values were corrected for multiple hypothesis testing using the Benjamini and Yekutieli multiple hypothesis correction, and, if relevant, the significant relationships (FDR 5%) were further characterized using Tukey honest significant differences computation. The increase in heterogeneity following inhibition was quantified by comparing the average standard deviation of the median fold change at 60 minutes with ANOVA followed by Benjamini and Yekutieli multiple hypothesis correction for the six treatments.

Mass spectrometry data analysis

DIA-MS targeted data extraction

Targeted data extractions of DIA-MS acquisitions were performed with Spectronaut Pulsar (11.0.18108.11.30271 Asimov, Biognosys AG) with default settings (Bruderer et al., 2015). Retention time prediction was set to dynamic with correction factor 1 for XIC extraction window determination. Non-linear calibration was used for retention time correction, and MS2 level interference correction was enabled (Bilbao et al., 2015). The FDR was set to 1% at peptide precursor level and was estimated with mProphet (Reiter et al., 2011). The method compares time-resolved MS/MS maps measured with the DIA-MS method as previously described (Gillet et al., 2012).

Quantification

Subsequently the data were analyzed with *MSstats* (using Tukey's median polish, R package version 3.10.6) for differential protein abundance in comparison to five cell lines derived from normal breast tissue (184A1, 184B5, MCF10A, MCF10F, and MCF12A) (Choi et al., 2014). For quantification, only proteotypic peptides, which are uniquely present in the sequence of one protein, were used. The default settings for *SpectronauttoMSstatsFormat* and the *dataProcess* functions were used with the exception that the normalization was provided by Spectronaut Pulsar and zero intensities were censored. For each cell line comparison, MSstats (with the *groupComparison* function) was used to determine model-based estimates of fold changes. The adjusted p-values were determined using the Benjamini-Hochberg method to control the FDR at the cut-off level of 0.05 (Benjamini and Hochberg, 1995). Proteins with a fold

change of at least 2 were considered as differentially abundant. For plotting, *-Inf*, *NA*, and *Inf* values were set to the dataset's minimum, zero, and maximum, respectively.

Gene ontology enrichment analysis

The Gene Ontology (GO) enrichment analysis was performed using the GOATOOLS Python-based library (Klopfenstein et al., 2018). The background set corresponds to all human proteins (https://www.ncbi.nlm.nih.gov/genome/51, genome annotation file downloaded on May 12, 2015). The option *propagate_counts* was set to *False* to avoid propagation of the annotations of a gene from the assigned GO category to all parent GO terms. The p-value was calculated using Fisher's exact test and then adjusted for multiple testing using the Benjamin-Hochberg correction method (Benjamini and Hochberg, 1995). We next calculated the specificity of the enriched GO terms by computing their information content (IC) as follows: IC = −log (frequency), where frequency is the number of genes annotated to the current GO term divided by the total number of associations between genes and GO terms in the full branch. The semantic similarity between all the enriched GO terms was then calculated as the inverse of the semantic distance (number of branches separating the terms). The IC and semantic similarity values were finally used to filter the list of GO-enriched categories selecting the more informative GO term (highest IC) among pairs of terms showing a semantic similarity higher than 0.5. To visualize the results of the functional enrichment analysis across the 62 tumor-derived cell lines, GO terms with a number of associated genes larger than 500 or smaller than 100 as well as terms commonly enriched in less than 10 cell lines were excluded to reduce the complexity and the redundancy of the plot while preserving the biological outcome.

Drug sensitivity feature importance

The procedure for estimating the feature importance was as follows:

1. For every MCMC sample, we:
   a. Extracted the latent vector $V_{drug\ 1}$ for a given drug number 1. This latent vector represented a subset of L_{drug} for a specific drug 1.
   b. Extracted the link matrix of the cell-line side, $Link_{cell}$.
   c. Computed the element-wise multiplication: $V_{drug\ 1}$ * $Link_{cell}$. The resulting matrix represents the feature importance of the predictors for each latent dimension.
2. For each predictor, averaged across all L latent dimensions, we:
   a. Took the average feature importance across all cross validations and over 40 iterations.
   b. Generated random permutations of the feature importance matrix for all drugs 1,000 times, where we shuffled the predictors for each cell line independently. We then derived an empirical null distribution for each feature importance value. If the value was positive, we defined the p-value as the number of cases in the null distribution greater than the value of interest divided by the number of permutations. If the value was negative, we defined the p-value as the number of cases in the null distribution smaller than the value of interest divided by the number of permutations.

Features predictive of overall sensitivity

To determine features that significantly predicted overall sensitivity we performed an ANOVA with H_0: effect size > 0.01 or < -0.01 across all drugs and conditions for the predictors: median, cellular variability, and edge flux. The obtained p-values were corrected for multiple hypothesis using Benjamini and Yekutieli (features * 2).

Features predictive of pathway sensitivity

Drugs were binned in different classes according to the target pathway (Yang et al., 2013). Upon selection of ten interesting classes we looked for features predictive for these specific dug classes with an ANOVA with H_0: effect size > 0.01 or < -0.01. The threshold for large effect size was arbitrarily set at 0.1. The obtained p-values were corrected for multiple hypothesis testing using Benjamini and Yekutieli (features * 2), and the significant relationships (FDR 5%) were further dissected using Tukey honest significant differences computation.

Comparison of the two QTL approaches

The genomic features (independently for SNPs and CNAs) passing the 0.3 adjusted *p-value* cutoff were subsequently tested for effects on the drug sensitivity (IC_{50} values (*–ln*) for pictilisib, fulvestrant, and lapatinib) by using ANOVA. The ANOVA was performed only when the genomic feature identified by QTL was linked to a signaling feature predictive of the sensitivity of the specified drug (p-value $\leq$ 0.005 and effect size $\geq \pm$ 0.02, see the section "Feature Importance"). The p-values obtained by the ANOVA were then corrected for multiple hypothesis testing for each drug individually (Benjamini and Hochberg, 1995).

Comparison of PDTX to the cell line data

We assessed the associations between CNAs and drug sensitivity that had been predicted by our cell line-based signaling model as follows. First, we filtered both the *in vitro* (cell line) and *in vivo* (PDTX) data for only those comparisons of CNA-call status with at least four drug sensitivity measurements in each dataset. Second, for those gene-drug relationships passing this threshold, we performed

an ANOVA followed, if necessary, by Tukey honest significant differences computation to define which specific relationships (i.e., drug sensitivity for amplification versus loss or drug sensitivity for amplification versus wild type) were affected. We conducted the same type of analysis for the top CNA-drug sensitivity associations that had been predicted by direct QTL. For this comparison, we considered the three best gene candidates (ranked by *q*-value) from the QTL analysis; in the cases where there were multiple genes with the same *q*-value, we included all genes at that rank. We then proceeded with the comparison using the same filtering and testing criteria as for the genotype-drug sensitivity associations as described above.